International Journal of Mining Science and Technology 35 (2025) 1827–1843

Contents lists available at ScienceDirect

International Journal of Mining Science and Technology

journal homepage: www.elsevier.com/locate/ijmst

Experimental investigation on failure mode and fracture characteristic of rock samples induced by laser irradiation

Dongxu Yu [a], Yijiang Wang [a,b,*], Shuchen Li [a], Zongheng Jiang [a], Jianzhou Wang [a]

[a] State Key Laboratory of Intelligent Construction and Healthy Operation and Maintenance of Deep Underground Engineering, School of Mechanics and Civil Engineering, China University of Mining and Technology, Xuzhou 221116, China
[b] Yunlong Lake Laboratory of Deep Underground Science and Engineering, Xuzhou 221116, China

ARTICLE INFO

Article history:
Received 17 July 2025
Received in revised form 1 September 2025
Accepted 3 October 2025
Available online 25 October 2025

Keywords:
Laser irradiation
Fracture surface roughness
Pore distribution
Acoustic emission

ABSTRACT

For hard rock cracking induced by laser irradiation, the failure modes and fracture characteristics among rocks of different types and sizes are still unclear. Therefore, the experiments on laser-induced fracturing of limestone, sandstone, and various-sized granite specimens were conducted. Real-time acoustic emission monitoring and laser scanning were employed to capture acoustic emission signals inside rocks during laser irradiation and to reconstruct the fracture surfaces after laser irradiation. Results indicate that abundant melts in sandstone and granite dissipated laser energy, leading to lower acoustic emission peak energy compared to limestone. Larger-sized specimen delayed the occurrence of peak energy. Crystal thermal expansion and changes in pore pressure induced tensile-shear composite failure in limestone, whereas thermal expansion of minerals in sandstone and granite promoted tensile failure. Fracture surface morphology was influenced by sampling interval, anisotropy, and size effects. The joint roughness coefficient and fractal dimension of sandstone exceed granite and limestone. Asperity heights and slope angles ranged from 1–14 mm and 0–40°, respectively, with the average aspect angles exceeding 110°. Granite exhibited the highest proportion of macropores after laser irradiation, approximately 4.8%. These findings provide valuable insights for the application of laser-assisted fracturing in hard rock excavation.

1. Introduction

Tunnel boring machines (TBMs) serve as the primary mechanism for hard rock excavation during tunneling. However, when dealing with high-strength rock masses, TBMs encounter significant challenges, including elevated specific energy requirements, diminished advance rates, pronounced cutter wear, and construction delays. These issues not only escalate operational costs but also heighten project risks [1]. For example, in the Floskefonn Tunnel (Norway), rock exhibiting a compressive strength of 270 MPa decelerated the TBM's advance rate to a mere 0.5 m/h [2]. Similarly, in the Qinling Water Diversion Tunnel (China), rocks with a compressive strength reaching up to 325 MPa curtailed advance rates to 1.2 m/h, resulting in monthly progress of less than 170 m [3]. Analogous challenges have been documented in India, South Africa, and Turkey [2]. Consequently, tunneling through such exceptionally hard rock formations presents a formidable global challenge in the realm of deep underground engineering. There is an imperative need to innovate rock fragmentation technologies tailored for these demanding formations.

The development of advanced rock-breaking methodologies is critical for overcoming issues including low advance rates, accelerated cutter wear, and high costs in high-rock excavation [4]. Numerous innovative rock-breaking technologies are under extensive investigation, including microwave, water-jet, and laser [3]. Among these, laser fracturing technology is perceived as a promising alternative due to its non-contact method and environmentally friendly advantages [5]. This technology converts electrical energy into thermal energy, which is then concentrated on the rock surface. This generates intense thermal effects, inducing the weakening, fragmentation, melting, and gasification of rock minerals. These processes generate new free surfaces that reduce their fragmentation resistance. Studies have demonstrated that the temperature gradient within a rock sample induced by laser irradiation reached 5000 °C/mm, leading to a reduction in compressive strength by 69% [6]. Li et al. [7] reported that the thermal stress induced in rock specimens under laser irradiation ranges from 481 to 536 MPa, which substantially exceeds the strength threshold of the rock and results in rock failure. Li et al. [8] revealed that

* Corresponding author.
E-mail address: yjwang@cumt.edu.cn (Y. Wang).

https://doi.org/10.1016/j.ijmst.2025.10.001

laser-induced rock damage is essentially a dynamic process involving the initiation, propagation, and coalescence of internal cracks. Chen et al. [9] demonstrated that tensile stress dominates rock failure during laser exposure. As thermal stress accumulates and propagates, the thermal damage intensifies. This process drives stress redistribution within the rock, ultimately triggers energy release through thermal cracking.

Existing studies have demonstrated that laser irradiation induces an ultrahigh temperature rise rate exceeding 300 °C/ms in rock, representing a typical thermal shock effect [10]. Thermal shock in rocks induces thermal expansion mismatches among minerals, leading to microcracks initiation and elastic waves. Acoustic emission (AE) techniques are widely applied to assess microcrack propagation within rocks through monitoring the elastic waves. Feng et al. [11] found that variations in AE parameters can reflect the damage evolution behavior within rocks after laser irradiation. Gao et al. [12] reported that rock releases numerous AE events and high AE energy at the instant of failure after irradiation. Zhou et al. [13] revealed that the AE energy distribution exhibits good consistency with crack distribution. Chen et al. [9] reported that laser-induced damage in rock primarily manifests as the generation of thermal cracks. The rock delayed tensile failure due to the stress concentrations at the crack tips. Laser irradiation predominantly generates tensile cracks in the rock, with shear cracks being secondary. The ratio of average frequency (AF) to rise angle (RA) is commonly applied to classify cracks during rock failure [14]. The conventional classification method employs a 45° line. Wang et al. [15] discovered that AE signals generated during tensile failure typically exhibit higher AF values and lower RA values, whereas shear failure signals with lower AF values and higher RA values. Qin et al. [16] observed that, with increasing temperature, the share of tensile cracks within rocks decreases while the share of shear cracks increases. Although numerous studies have investigated AE monitoring during rock failure, research on AE characteristics during laser-induced rock fracturing remains insufficient.

The characterization of rock fracture surfaces is essential for comprehending the mechanism underlying rock fracture [17,18]. Researchers typically employ the joint roughness coefficient (JRC), fractal features to evaluate the roughness of these surfaces. Gu et al. [19,20] demonstrated that the accumulation of damage within rock subjected to thermal cycling induces notable alterations in the roughness, anisotropy, and aperture of fracture surfaces. Li et al. [21] discovered that the fracture surfaces with greater fractal dimensions were affected by a great share of tensile fractures throughout the formation process, as evidenced by true triaxial tests. Yang et al. [22] reported that the asperity height of the rock fracture surface was in the range of 1–7 mm subsequent to microwave treatment. Moreover, the rough fractal dimension exhibited a positive correlation with the sample size. Yang et al. [23] demonstrated that the fractal dimension elevated with prolonged microwave treatment and that water-cooled samples exhibited higher fractal dimensions compared to air-cooled samples. Aghababaei et al. [24] reported that the sensitivity of fracture surface roughness parameters was significantly affected by sample interval, with increased fracture surface roughness correlating with larger grain sizes. Despite extensive research on the roughness features of rock fracture surfaces following microwave treatment, Brazilian splitting, and uniaxial compression, there is a remarkable paucity of studies inspecting the roughness features of rock fracture surfaces induced by laser irradiation.

Elucidating the pore distribution characteristics in thermally treated rocks provides potential evidence for probing the damage mechanisms underpinning microcrack behaviors and failure modes. Zhou et al. [13] reported that laser irradiation predominantly created pores in basalt within the 0.025–0.500 μm range, comprising approximately 71.6% of the total pore volume. Utilizing nuclear magnetic resonance (NMR), Pan et al. [25] assessed the pore-size distribution in laser-irradiated rocks and observed that the combined proportions of macropores and mesopores exceeded 50%. Wu et al. [26] found that laser irradiation triggered the coalescence of micropores and mesopores in granite, leading to an increase in the macropore fraction by roughly 19%. This amplified internal damage, culminating in rock failure. Zhang et al. [27] delineated four stages in the evolution of internal pores in sandstone exposed to microwave irradiation: overall pore expansion, localized pore closure in the internal zone, propagation of thermal stress-induced microcracks, and the development of macroscopic cracks. Yang et al. [28] observed that following temperature treatment at 600 °C, a decrease in cooling medium temperature resulted in a reduction in isolated pores and an increase in the fractal dimension within sandstone. Simultaneously, the total porosity, pore volume fraction, and permeability increased by 2.88%, 7.55%, and 49.4%, resulting in more severe damage within the sample. Although the effects of heat and microwave treatment on rock pore distribution have been extensively studied, investigations into the pore distribution of different rock types under laser irradiation remain limited.

Numerous studies have focused on the AE responses, fracture surface features, and pore evolution of rocks subjected to mechanical testing and microwave irradiation. However, there is a significant lack of investigations demonstrating the real-time AE signals, fracture surface characteristics, and pore distribution of rocks irradiated by laser. Therefore, this study conducted laser cracking tests on limestone, sandstone, and various-sized granite specimens, and captured the real-time AE signals. Furthermore, it analyzes the morphological and anisotropic properties of rock fracture surfaces and investigates the pore distribution patterns within rocks after laser irradiation. The results could offer valuable insights for the adoption of laser fracturing technology in hard rock excavation.

2. Experimental methods

2.1. Specimen

The limestone samples employed in this study were collected from a fresh rock wall of the Majiagou Formation (Ordovician) in Xuzhou, Jiangsu Province. The rock mass shows a dense structure with visible calcite veinlets. The sampling location exhibited intact lithology with poorly developed fractures and no visible weathering. The sandstone specimens were taken from a fresh outcrop of the Maoshan Formation (Silurian) in Suzhou, Jiangsu Province. The rock has a uniform and compact granularity, showing minimal weathering and high integrity. The granite samples originated from the fine-grained monzogranite intrusion of the Yanshanian-period medium in Zhumadian City, Henan Province. The rock displays a dense, massive structure and homogeneous granular texture, with negligible signs of weathering. As depicted in Fig. 1, the flatness of the end faces of all rock specimens was maintained at less than 0.02 mm. The diameter-to-height ratio of the rock samples was standardized at 2:1, as detailed in Table 1. All limestone and sandstone specimens were processed into cylindrical specimens with dimensions of ϕ50 mm × 25 mm. A portion of the granite specimens was also processed into ϕ50 mm × 25 mm, while the remaining samples were prepared in sizes of ϕ60 mm × 30 mm, ϕ80 mm × 40 mm, and ϕ100 mm × 50 mm.

The microstructures of granite, sandstone, and limestone specimens, as observed through scanning electron microscope (SEM), are presented in Fig. 2. It reveals that significant differences exist in the microstructures of the three rock specimens. The microstructure of the granite is planar, characterized by mineral particles with diameters of approximately 5 μm. The sandstone

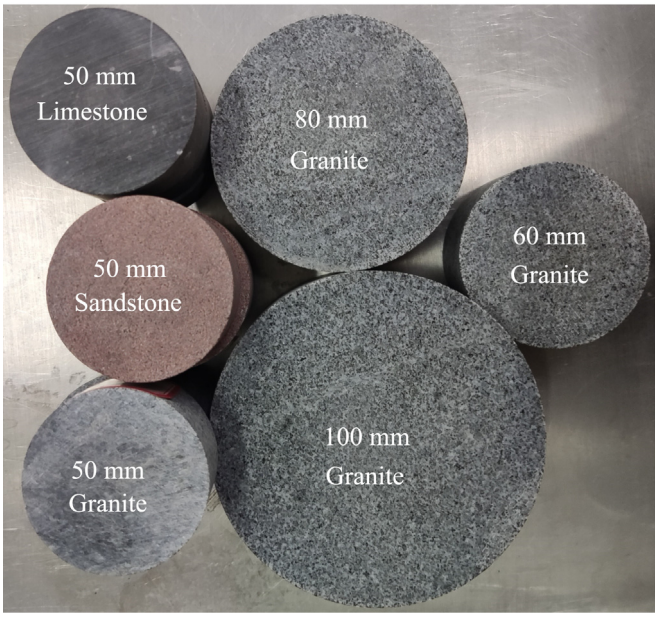

Fig. 1. Rock samples.

contains numerous initial pores, with diameters smaller than 1 μm and no mineral particles identified. The limestone is characterized by a significant concentration of well-organized calcite particles, with minimal presence of micropores and fractures.

Table 2 details the primary mineral components and mass fractions for rocks, as determined through an energy-dispersive spectrometer. In granite, quartz and plagioclase account for 15.1% and 77% of total mineral content, respectively. Whereas in sandstone, the proportions of quartz and plagioclase are 27.1% and 71.5%, respectively. Both granite and sandstone also contain trace amounts of minerals, such as biotite and anorthite. The predominant component of limestone is calcite, comprising approximately 89.26%, alongside minor inclusions of quartz and other minerals.

2.2. Experimental instruments and scheme

The laser-cracking experiments were performed utilizing the three-dimensional fiber laser system as depicted in Fig. 3a. The system operates at a laser wavelength of (1080±10) nm, achieving a maximum output power of 1000 W. The OKIO-H-200 3D laser topography scanner, manufactured by Beijing TenYoun Technology Co., Ltd., was utilized to acquire morphological data of rock fracture surface, achieving a scanning accuracy between 0.002 –0.01 mm, as shown in Fig. 3b. The MesoMR23-060 V-I nuclear magnetic resonance system, developed by Suzhou Niumag Corporation, was utilized to assess the pore distribution of the rocks. The system maintained a magnetic field strength of (0.5±0.05) T, as indicated in Fig. 3c. The microscopic structural morphology of the rock was characterized using the GAIA3 XMH focused ion beam SEM, manufactured by TESCAN. In high vacuum mode, this SEM achieves a resolution of 0.7 nm at 15 kV, as illustrated in Fig. 3d. The AE signals generated during laser-induced rock fracturing were monitored employing a PCIe-Q87-i2m AE system (Physical Acoustics Corporation, USA), as illustrated in Fig. 3e. Vaseline was utilized as a coupling agent, facilitating the connection between the AE sensors and the specimen. To minimize external disturbances, the experiments were conducted in a tranquil laboratory setting. The AE acquisition threshold was also established at 40 dB [29].

Prior to conducting the laser-irradiation test, specific parameters were set, including a power setting of 1000 W, an irradiation time of 30 s, and a defocus distance of 6 cm. To ensure uniformity in the defocus distance among rock specimens of varying sizes, the position of the laser cutting head was adjusted accordingly. Additionally, two sensors were utilized in each test to continuously monitor the real-time AE signals. These probes were installed at identical heights and positioned in pairs along the diameter direction of the sample. Consequently, the linear distance between the two sensors corresponded to the sample's diameter. Following the laser-induced thermal cracking tests, a three-dimension laser topography scanner was employed to capture the fracture surfaces of all irradiated specimens. The resulting point cloud data were split into grid units of 0.1 mm × 0.1 mm using the Kriging interpo-

Table 1
Sizes and strength of rock samples.

Diameter (mm)	Height (mm)	Index	Tensile strength (MPa)	Rock type
50	25	L1	3.6	Limestone
50	25	S1	3	Sandstone
50	25	G1	10.2	Granite
60	30	G2	4.7	Granite
80	40	G3	3.2	Granite
100	50	G4	3.1	Granite

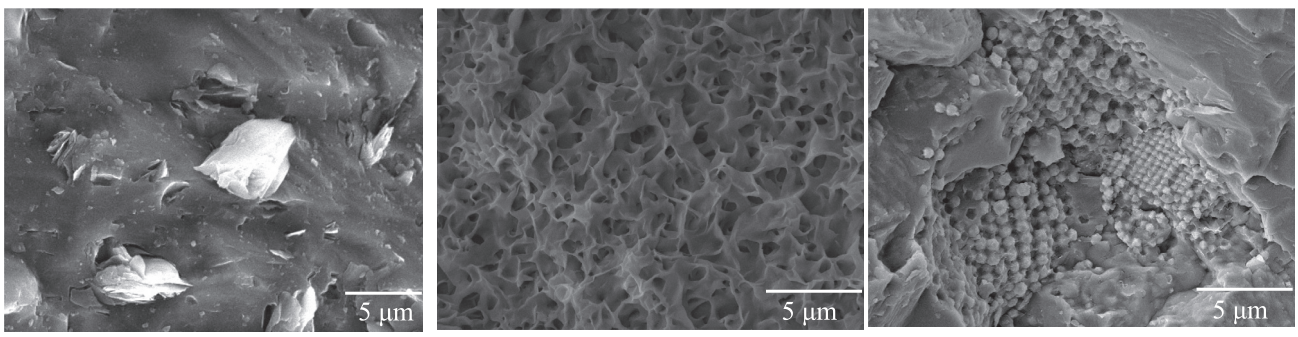

(a) Granite (b) Sandstone (c) Limestone

Fig. 2. Microstructure of original rock specimens.

Table 2
Mineral composition of granite, sandstone and limestone, %.

Composition	Quartz	Plagioclase	Biotite	Calcite	Anorthite	Other
Granite	15.1	77	7.2	0	0	0.7
Sandstone	27.1	71.5	0	0	0.8	0.6
Limestone	6.21	0	0	89.26	0	4.53

lation method combined with grid sparsity processing. Subsequently, the data were refined using CloudCompare. The reconstruction and quantitative analysis of the fracture surfaces were performed utilizing Surfer software.

2.3. Data processing

(1) Joint roughness coefficient.

The JRC is frequently employed to depict the contour roughness of rock fracture surfaces. The fracture surface is segmented into equidistant contour lines radially. The mean JRC of all contour lines is considered as the JRC of the entire fracture surface. The JRC is computed by Eqs. (1) and (2) [20]:

$$\mathrm{JRC} = 32.2 + 32.47\log_{10} Z_2 \tag{1}$$

$$Z_2 = \left[\frac{1}{M}\sum_{m=1}^{M-1}\left(\frac{Z_{m+1} - Z_m}{\Delta x}\right)^2\right]^{\frac{1}{2}} \tag{2}$$

where Z_2 is the root mean square of the first-order differences of the coordinates in the 2D nodes; Z_m and Z_{m+1} the heights of points m and m + 1 in the cloud data of the sample surface, mm; M the sum of sampling numbers; and Δx the sampling step.

(2) Fractal dimension

The cube-counting algorithm is applied to obtain the fractal feature of cracked surfaces in this study. The fractal dimension (D_r) is computed as follows [23]:

$$D\_r = -\lim_{\xi \to 0} \frac{\log N(\xi)}{\log(\xi)} \tag{3}$$

where ξ is the length of the edge of cubes, mm; $N(\xi)$ is the number of cubes.

(3) Aspect angle, asperity height, and slope angle.

The aspect angle is determined as the degree between the projection of the unit perpendicular vector along the XY plane and the positive X-axis, as estimated by Eq. (4):

$$b = \arccos < \boldsymbol{e}_\mathrm{n}, \boldsymbol{u}_\mathrm{n} >= \frac{\boldsymbol{e}_\mathrm{n} \cdot \boldsymbol{u}_\mathrm{n}}{|\boldsymbol{e}_\mathrm{n}| \cdot |\boldsymbol{u}_\mathrm{n}|} \tag{4}$$

where b is the aspect angle, (°); $\boldsymbol{u}_\mathrm{n}$= (1,0,0), a direction vector along the X-axis; and $\boldsymbol{e}_\mathrm{n}$ the projection vector of $\boldsymbol{c}_\mathrm{n}$ onto the XOY plane.

The asperity height of the fracture surface is described as the node height of the fracture surface unit, and the slope angle is determined as the angle between the unit's normal vector and the Z-axis, which is computed as follows [30]:

$$a = \arccos < \boldsymbol{c}_\mathrm{n}, \boldsymbol{v}_\mathrm{n} >= \frac{\boldsymbol{c}_\mathrm{n} \cdot \boldsymbol{v}_\mathrm{n}}{|\boldsymbol{c}_\mathrm{n}| \cdot |\boldsymbol{v}_\mathrm{n}|} \tag{5}$$

where a is the slope angle, (°); $\boldsymbol{v}_\mathrm{n}$= (0,0,1), a direction vector of the Z-axis; and $\boldsymbol{c}_\mathrm{n}$ the normal vector of grid nodes, calculated by Eq. (6):

$$c_\mathrm{n} = \frac{\boldsymbol{q}_1 \times \boldsymbol{q}_2}{\| \boldsymbol{q}_1 \times \boldsymbol{q}_2 \|} \tag{6}$$

where $\boldsymbol{q}_1$, $\boldsymbol{q}_2$ are the direction vectors of the element nodes along the X- and Y-axes, respectively, computed by Eqs. (7) and (8).

$$\boldsymbol{q}_1 = \{[\boldsymbol{X}(s+1,t), \boldsymbol{Y}(s+1,t), \boldsymbol{Z}(s+1,t)] - [\boldsymbol{X}(s,t), \boldsymbol{Y}(s,t), \boldsymbol{Z}(s,t)]\} \tag{7}$$

$$\boldsymbol{q}_2 = \{[\boldsymbol{X}(s,t+1), \boldsymbol{Y}(s,t+1), \boldsymbol{Z}(s,t+1)] - [\boldsymbol{X}(s,t), \boldsymbol{Y}(s,t), \boldsymbol{Z}(s,t)]\} \tag{8}$$

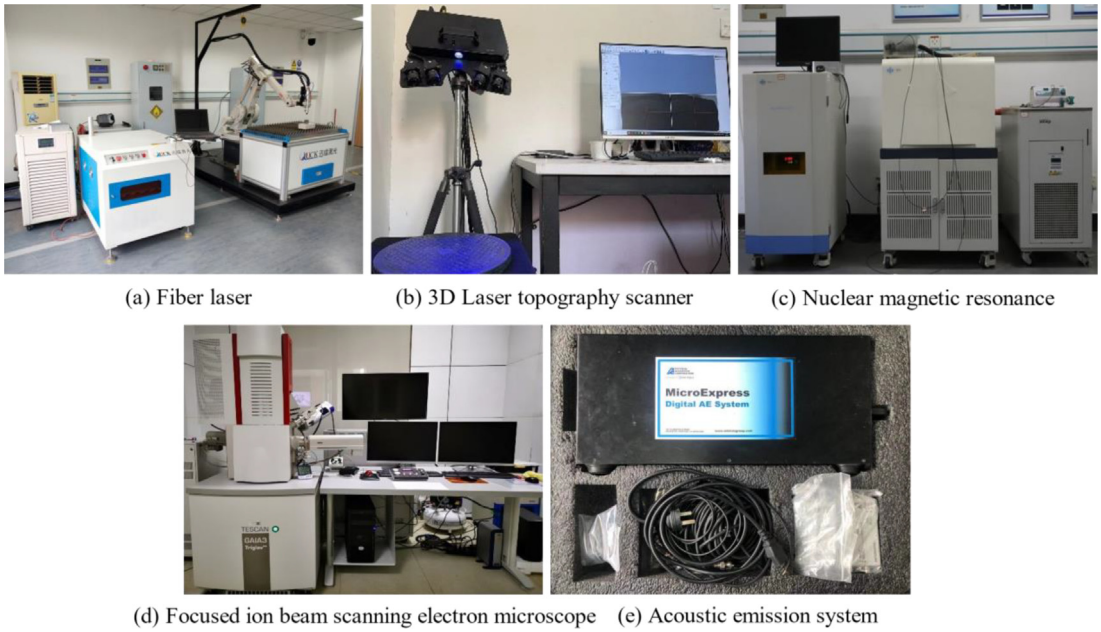

(a) Fiber laser (b) 3D Laser topography scanner (c) Nuclear magnetic resonance

(d) Focused ion beam scanning electron microscope (e) Acoustic emission system

Fig. 3. Experimental instruments.

where the matrices $\boldsymbol{X}(s,t)$, $\boldsymbol{Y}(s,t)$, and $\boldsymbol{Z}(s,t)$ are the location values of the *X*-, *Y*-, and *Z*-axes, respectively.

3. Results and discussion

3.1. Failure mode

3.1.1. Acoustic emission energy

Fig. 4 illustrates the variation in real-time AE energy during laser-rock interaction. Fig. 4a presents the AE energy curves versus laser irradiation time for L1, S1, and G1, respectively. The AE energy curve of sandstone exhibits distinct oscillating characteristics, followed by granite, while limestone displays a relatively smooth AE signal. This may be attributed to the greater density of initial pores within the sandstone. The stress concentration induced by laser irradiation at the tips of micropores triggers microcrack initiation and generates AE signals [31]. Furthermore, phenomena such as melting, vaporization, and melt ejection occurring in granite under laser irradiation produce detectable AE signals. Limestone primarily undergoes the decomposition reaction under laser impact, resulting in fewer captured AE signals. However, limestone manifests higher peak AE energy compared to sandstone and granite. Specifically, the peak AE energies for limestone, sandstone, and granite are 3008.6, 1464.8, and 1750.8 mV/μs, respectively. This difference arises from the decomposition reaction of limestone, which leads to more thermal energy being utilized in the laser fracturing.

Fig. 4b demonstrates the variation of AE energy with laser irradiation time for specimens G1, G2, G3, and G4. The results demonstrate that the timing of the peak AE energy occurrence delays as the size of the rock specimen increases. For instance, as the granite specimen size increases from ϕ50 mm × 25 mm to ϕ100 mm × 50 mm, the peak AE energy occurs at 21, 25, 27, and 33 s, respectively. Furthermore, the peak AE energy increases with increasing specimen size. Specifically, peak AE energies for specimens G1, G2, G3, and G4 are 1750.8, 1897, 3960, and 4348.7 mV/μs, respectively. This indicates that laser-induced fracturing of larger specimens requires greater energy consumption.

3.1.2. Crack distribution

As illustrated in Fig. 5, RA represents the ratio of rise time to peak amplitude, while AF denotes the ratio of AE counts to duration time [32]. The diagonal slope in RA-AF distributions is conventionally adopted as the criterion for distinguishing tensile from shear cracks. Calculated values falling below this slope threshold typically indicate shear failure, whereas those exceeding it correspond to tensile failure. A uniform threshold of 10/3 was established for all rock samples, based on the computed ranges of AF and RA values. This approach ensures both consistency and comparability across the different samples.

Fig. 6 presents the crack classification results derived from division using the 45° line. Fig. 6a–c illustrates the crack classification results for sandstone, limestone, and granite, respectively. The results reveal that the RA values for three types of rock samples

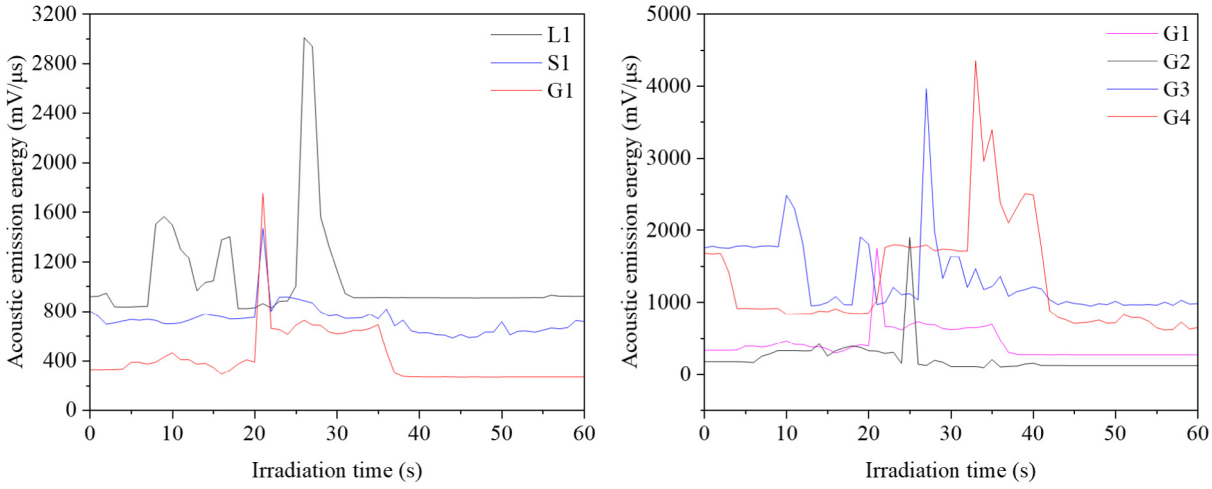

(a) Different types of rocks (b) Various-sized granite specimens

Fig. 4. Real-time acoustic emission energy of rock samples.

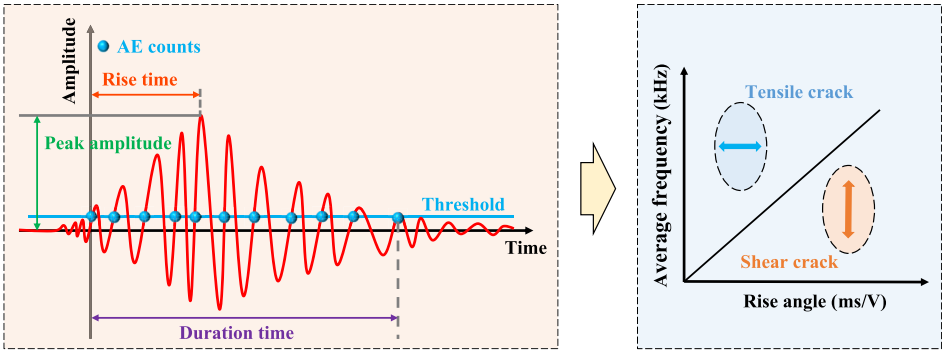

Fig. 5. The failure type of acoustic emission [32].

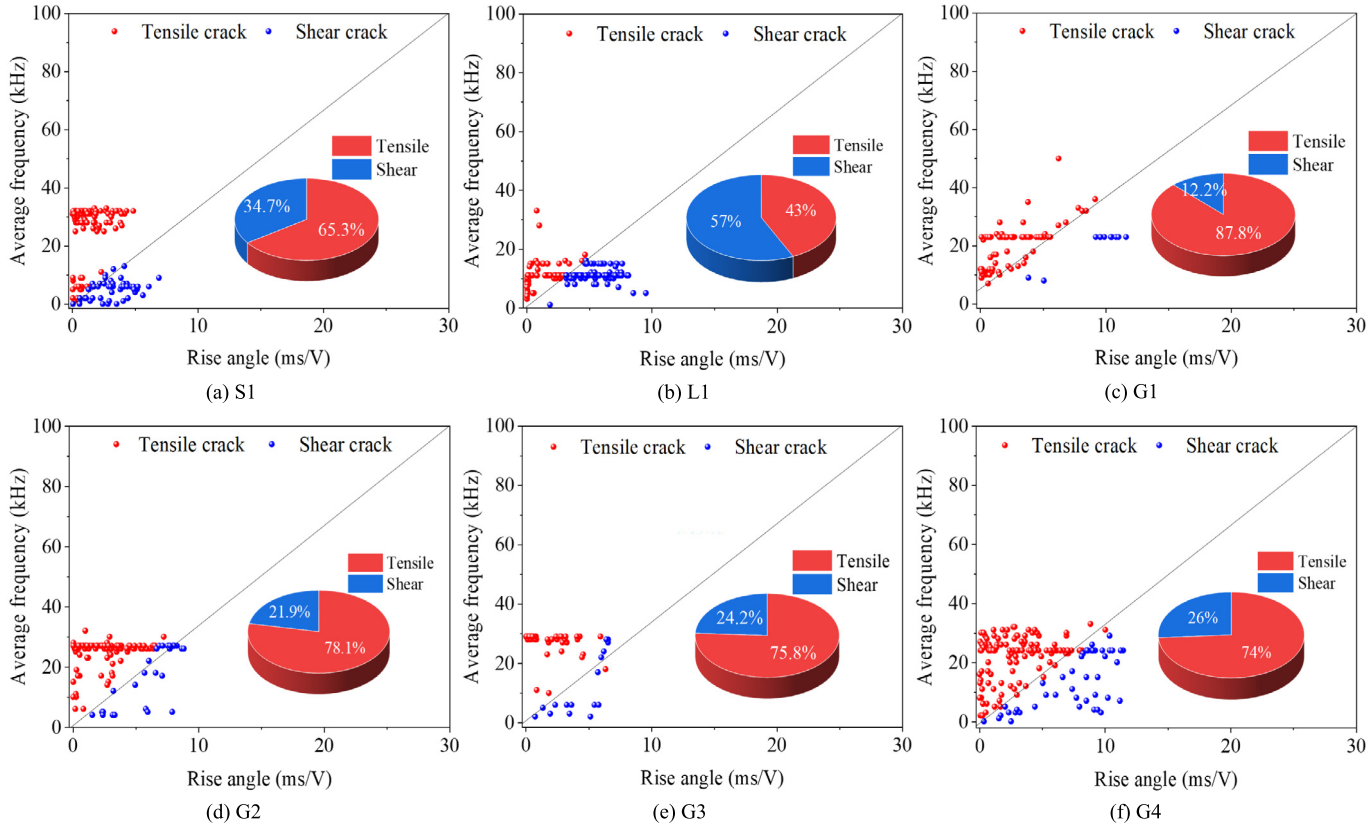

Fig. 6. Crack distribution within rocks.

predominantly range between 0–10 ms/V, while the AF values fall within the range of 0–100 kHz. Furthermore, the tensile cracks account for 87.8%, 65.3%, and 43% of the total cracks generated in granite, sandstone, and limestone, respectively. Meanwhile, the shear cracks constitute 12.2%, 34.7%, and 57% for these rocks, respectively. This indicates a tensile-shear mixed failure mode for limestone during laser irradiation, while granite and sandstone experience predominantly tensile failure. This observed dominance of tensile failure modes in sandstone and granite aligns with the findings from mechanical testing and crack distribution analyses reported by Liu et al. [31].

Fig. 6c–f depicts the crack classification results for granite specimens of varying sizes. The findings reveal that as the specimen dimensions increase from ϕ50 mm × 25 mm to ϕ100 mm × 50 mm, the RA values primarily distribute within 0–20 ms/V and the AF values predominantly fall within the range of 0–100 kHz. Additionally, it indicates that with specimen size increase, the share of tensile cracks decreases while the share of shear cracks rises. Specifically, the proportions of tensile crack are 87.8%, 78.1%, 75.8% and 74% for specimens G1, G2, G3, and G4, respectively, and a corresponding increase in shear crack proportion from 12.2% to 26%.

A conical hole appeared due to the melting and vaporization of rock specimens by laser irradiation. This hole introduced additional new free surfaces within the rock mass and promoted the crack propagation. Given that the tensile strength of rock is lower than its compressive strength, initial tensile cracks occur first under laser irradiation. As the irradiation time increases, these cracks extend inward and may deflect into type-II (tension-shear composite cracks generated by lateral deflection of type-I cracks toward one side) or type-III cracks (tension-shear composite cracks induced by lateral deflection of type-I cracks toward both sides simultaneously or successively) until macroscopic fracture occurs [31], signifying the rock failure. Additionally, as the irradiation time extends, shear cracks may also develop within the rock formation. The longer the time it takes for the rock to fail, the greater the proportion of shear cracks, driving a transition from predominantly tensile failure to a combined tensile-shear failure.

3.2. Fracture surfaces characteristics

3.2.1. Rock failure morphology

The rock morphology after laser cracking is presented in Fig. 7. The glassy material mainly accumulated on the rock surface following laser irradiation [33]. It could be easy to remove due to its properties, and the additional damage to the fracture surfaces could be negligible. Therefore, the glassy materials were manually removed to facilitate laser-scanning. It reveals that when disc-shaped rock is subjected to laser irradiation, the resulting cracks display clear type-I (tensile failure) characteristics. These fractures initiate as tensile cracks propagating vertically downward from the irradiated surface on the upper face of the rock. Under prolonged laser irradiation, type-I cracks could undergo deflection and evolve into type-II or type-III cracks [31]. In addition, the morphology of the reconstructed rock fracture surfaces is illustrated in Fig. 7. In this depiction, regions marked by blue indicate the lower height values on the fracture surface, whereas ones marked by red represent greater height values. It is significant to note that when the surface A of a particular rock exhibits a considerable height, the corresponding area on the surface B displays a lower height value. This suggests that the surface A and surface B of the same rock can be aligned to form a comprehensive rock fracture space after laser irradiation.

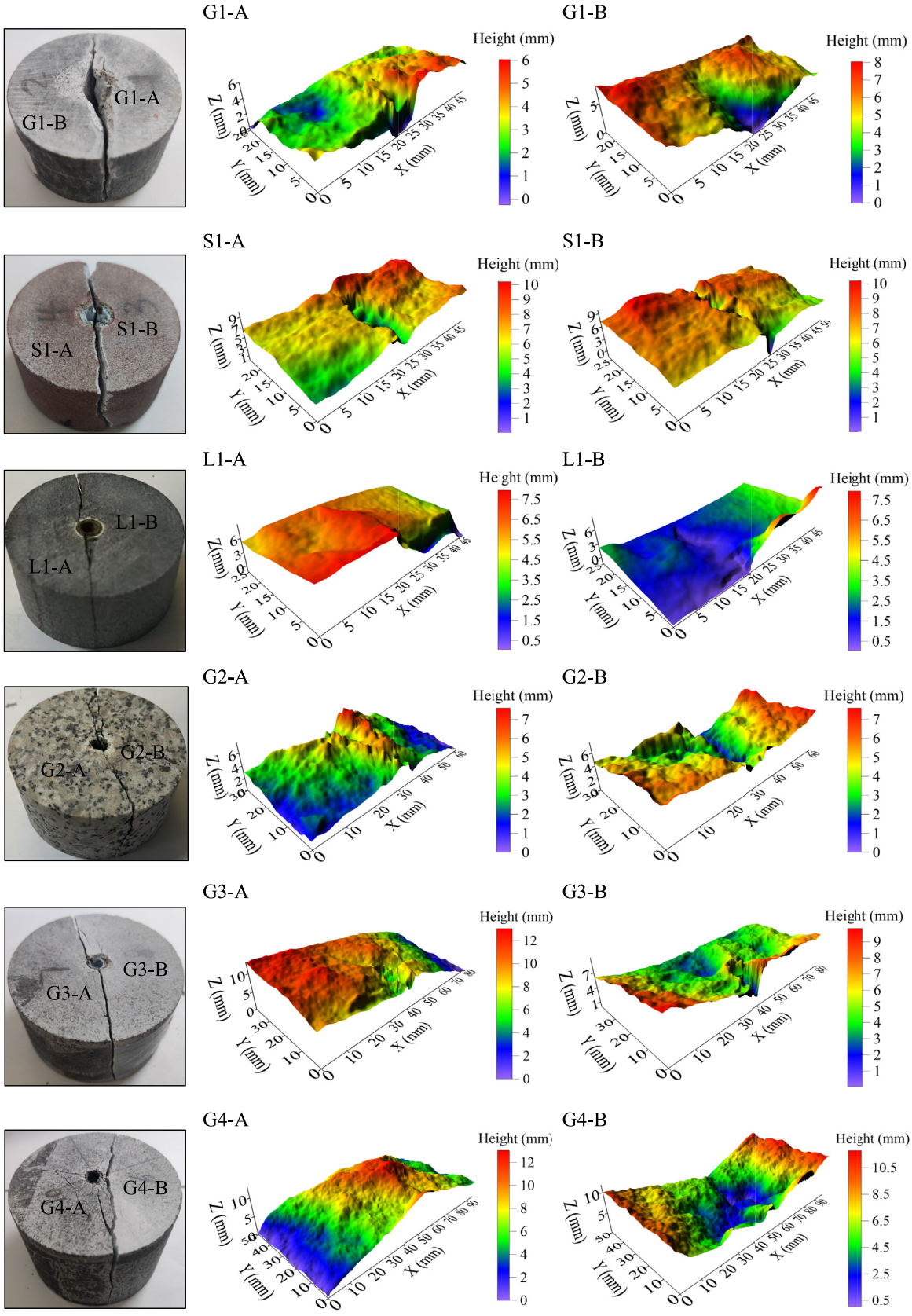

Fig. 7. Failure morphology of laser-cracked rock samples.

3.2.2. Joint roughness coefficient

Fig. 8 presents the JRC of fracture surfaces as calculated by Eq. (1). Fig. 8a illustrates the outcomes for the S1, G1, and L1 fracture surfaces. It is noted that the JRC value for sandstone exceeds that of granite and limestone at an equivalent sampling interval. For instance, at a sampling step of 0.5 mm, the JRC of the fracture surfaces of S1, L1, and G1 are 15.13, 11.37, and 11.5, respectively. This is due to that numerous initial micropores inside sandstone induce the deflection of microcracks and increase the randomness and disorder of microcrack propagation [34].

Fig. 8b displays the JRC values for the fracture surfaces of granite specimens with varying sizes. With a sampling interval of 0.5 mm, the JRC of the fracture surface increases from 11.5 to 13.5 as the granite diameter rises from 50 to 100 mm. This is owing to that the larger the granite specimen, the more likely it may contain more pre-existing defects, and the greater the possibility of inducing crack propagation. Under the action of laser thermal shock, tensile stress concentration will occur at the tip of microcrack defects within the rock, weakening the cementation between the mineral particles and impacting the height of the fracture surfaces [35].

Results demonstrated that thermally induced cracking significantly enhanced the roughness of rock fracture surfaces. The JRC of rock fracture surfaces from Brazilian splitting increased by approximately 58% and 30% through pretreatments including water saturation and freeze–thaw cycles, respectively [30,36]. Laser irradiation produced rock fracture surfaces with a JRC about 64% higher than that from Brazilian splitting. This trend is further supported by changes in fractal dimension. Following high-temperature and liquid-nitrogen-cooling cycles pretreatments, the fractal dimension of fracture surfaces increased by about 3.8%, whereas water saturation resulted in only a 0.3% increase [36,37]. Compared with Brazilian splitting, laser irradiation and microwave irradiation contributed to the increase in the fractal dimension by about 3.7% and 0.41%, respectively [23]. These findings indicate that the roughness of the rock fracture surface significantly depends on the treatment approaches.

3.2.3. Fractal dimension

Fig. 9 presents the results of the fractal dimension of fracture surfaces as calculated by Eq. (3). Fig. 9a illustrates the fractal features of sandstone, granite, and limestone fracture surfaces. The results convey that the fractal dimension of sandstone fracture surface exceeds those of both granite and limestone following identical laser incident conditions. Specifically, the fractal dimensions for the surfaces of specimens S1, G1, and L1 are 2.22, 2.129, and 2.097, respectively, with a sampling interval of 0.5 mm. This suggests that the crack propagation route in sandstone is more elaborate and winding compared to granite and limestone.

Fig. 9b displays the fractal features of the fracture surface for granite samples of varying sizes. The findings demonstrate a positive correlation between the granite size and the fractal dimension of the fracture surface, indicating that larger rock sizes correspond to higher fractal dimensions. Specifically, as a sampling interval of 0.1 mm, the fractal dimensions of the surfaces of G1, G2, G3, and G4 are measured to be 2.137, 2.183, 2.238, and 2.258, respectively. Significantly increasing the temperature induced by laser irradiation creates a differential in thermal expansion between granite mineral particles. This results in intergranular or even transcrystalline cracks at the boundaries of minerals and particles, coupled with the heterogeneity of particle distribution. These cracks make the granite sample more susceptible to tensile fracture [38].

The results depicted in Figs. 8 and 9 demonstrate a significant sampling interval effect on both the JRC and fractal dimension. This is manifested by a decrease in both the JRC and fractal dimension as the sampling intervals increase. For instance, in the G1 sample, as the sampling interval increases from 0.1 to 0.5 mm, the JRC of the fracture surface declines from 12.99 to 11.5, and the fractal dimension falls from 2.137 to 2.129. Similar trends are observed across fracture surfaces of other rock specimens. Furthermore, Xu et al. [35] reported that the sensitivity of parameters describing fracture surface morphology is significantly influenced by sampling size effects within a small sampling window. The smaller the sampling intervals, the sensitivities of different parameters to the sampling interval are more significant. Consequently, to mitigate the effect of sampling interval on these parameters, a sampling interval of 0.1 mm is recommended for all fracture surfaces of the specimens.

3.2.4. Aspect angle, asperity height, and slope angle

Aspect angle, asperity height, and slope angle serve as effective parameters for characterizing the nuance of rock fracture surfaces [22,23]. The surfaces A of all fractured rock specimens after laser

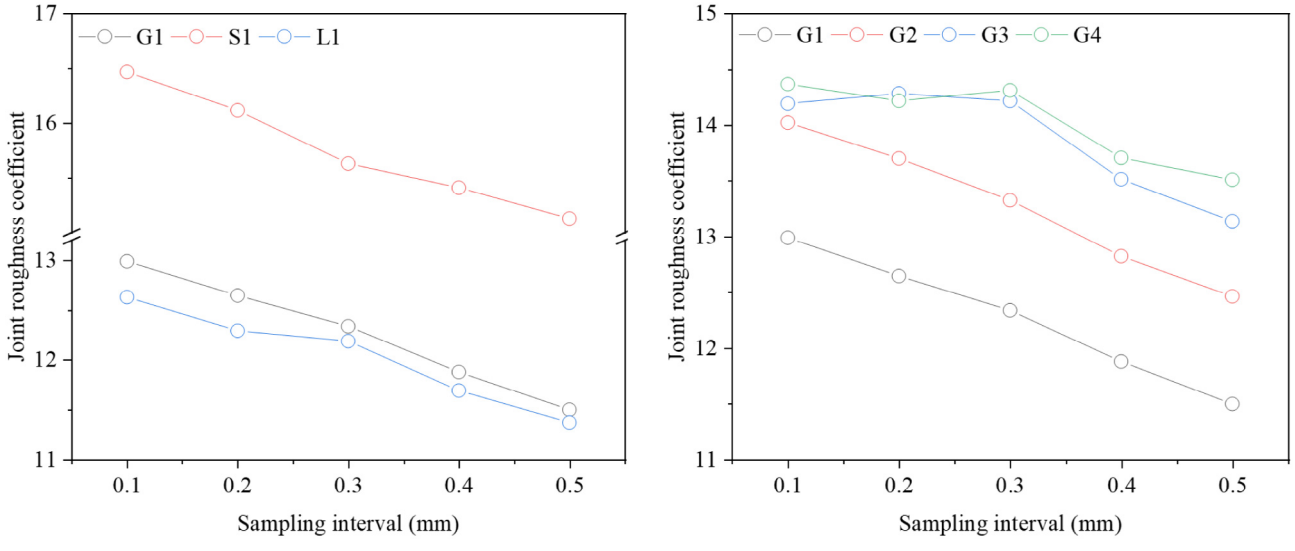

(a) Different types of rocks (b) Various-sized granite specimens

Fig. 8. Joint roughness coefficient versus sampling interval.

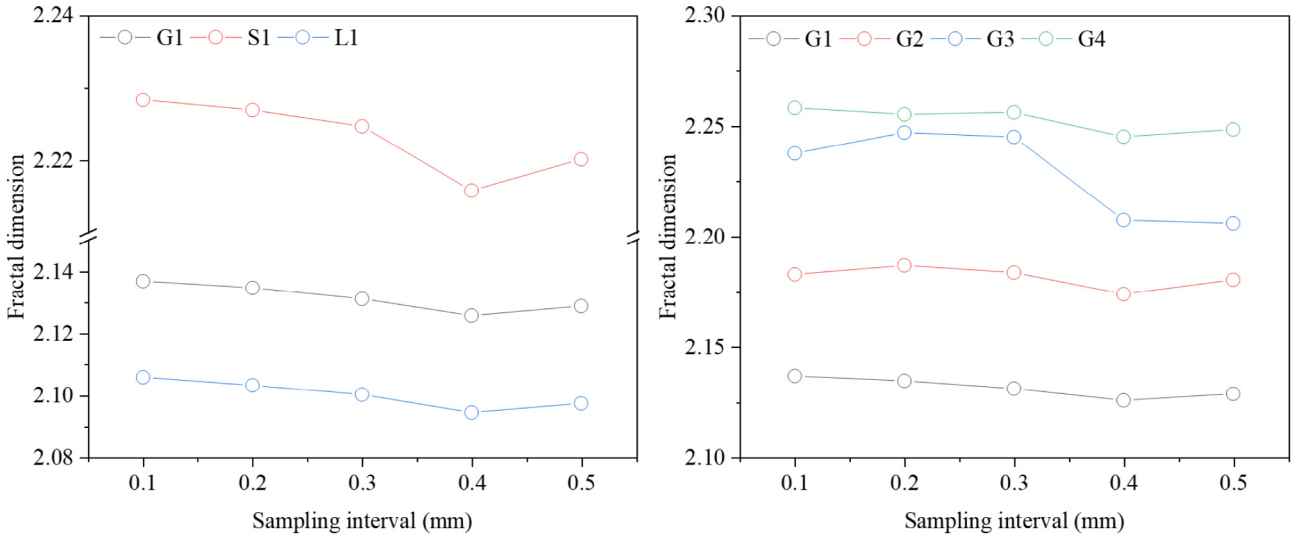

(a) Different types of rocks (b) Various-sized granite specimens

Fig. 9. Fractal dimension versus sampling interval.

irradiation were selected for quantitative analysis. To account for the differences between fracture surfaces and the impact of boundary effects on surface morphology, the absolute height was converted to relative height.

Fig. 10 illustrates the aspect angle distribution of fracture surfaces of rock. The data show that the average aspect angle of all rock fracture surfaces exceeds 110°, with a higher concentration of aspect angles observed within the intervals of 30°–105°, 135°–240°, and 315°–360°. It points out that following the laser irradiation, the roughness of the rock fracture surfaces within these specified ranges may be heightened.

Fig. 11 demonstrates the asperity height distribution across the fracture surfaces of irradiated rock. Fig. 11a–c presents the asperity height of L1, S1, and G1 fracture surfaces. The results suggest that the rock lithology significantly influences the asperity height of fracture surfaces. For instance, following laser irradiation, the asperity heights on the fracture surface of small-sized granite, sandstone, and limestone specimens predominantly range from 1 to 11 mm. Notably, the S1 fracture surface exhibits the largest standard deviation, approximately 1.53, indicating a greater degree compared to the granite and limestone fracture surfaces. This may be due to that the high temperature inside the rock caused by laser irradiation produces thermal stress. This process induces the development and expansion of microcracks and facilitates crack propagation and interconnection. Furthermore, the numerous initial pores in sandstone facilitate additional pathways for the extension and interconnection of microcracks, leading to increased complexity and tortuosity in crack propagation paths [34]. Consequently, the fluctuation of the asperity height for the sandstone fracture surface is broader than that of the granite and limestone.

Fig. 11c–f demonstrates the asperity height of granite specimens of varying sizes. The findings demonstrate that larger-sized granite fracture surfaces exhibit a larger range of asperity heights. For example, not only do the asperity heights of G3 and G4 fracture surfaces fluctuate between 0 and 14 mm, but also the standard deviations of asperity height of the fracture surfaces of G3 and G4 specimens are 2.96 and 2.71, respectively, which is greater than that of G1 and G2. This phenomenon is owing to that the increase of rock size results in the increase of ligament and thickness [39], thereby affecting the failure behavior of rock to some extent and subsequently influencing the asperity height of the rock fracture surface.

Fig. 12 presents the results regarding the slope angles of rock fracture surfaces. The results reveal that the slope angle distributions for small-sized rock fracture surfaces are more dispersed, whereas the distributions of larger-sized granite fracture surfaces are more concentrated. Specifically, the slope angles of surfaces of specimens S1, L1, G1, and G2 predominantly range from 0 to 40°, with standard deviations exceeding 11°, as presented in Fig. 12a–d. Nevertheless, the slope angles of surfaces of specimens G3 and G4 are concentrated between 60° and 90°, with an average slope angle greater than 60.5° as exhibited in Fig. 12e and f. This can be assigned to the increased presence of more internal defects in larger specimens, which facilitate additional paths for crack propagation and extension, thereby resulting in a greater inclination of the fracture surface. Furthermore, research conducted by Cao et al. [30] demonstrates that rock fracture surfaces subjected to heat-cold cycle treatment predominantly exhibited slope angles ranging from 0 to 40°, with an average value below 20°, akin to the slope angles observed in smaller-sized rock fracture surfaces under laser treatment.

Fig. 13 demonstrates the asperity height and slope angle of fracture surfaces of rock following laser irradiation. As illustrated in Fig. 13a, the rock fracture surfaces are categorized into three classifications based on the asperity height values: smooth surface (0–5 mm), moderately rough surface (5–10 mm), and rough surface (>10 mm). Results indicate that approximately 79.84% of the limestone fracture surfaces, when compared to granite and sandstone surfaces of equivalent size, fall within the 0–5 mm asperity height range, thereby categorizing them as smooth surfaces. The proportion of asperity height of 5–10 mm in granite and sandstone fracture surfaces is approximately 81.0% and 89.6%, respectively, categorizing them as moderately rough surfaces. Additionally, the fracture surfaces of G1 and G2 exhibit lower roughness levels than those of G3 and G4, which are classified as rough surfaces due to 45.9% and 14.2% of their asperity heights exceeding 10 mm, respectively. Wu et al. [40], Yang et al. [22], and Zhang et al. [41] performed investigations into the roughness variation of rock fracture surfaces subjected to Brazilian splitting under varying heat treatment temperature, microwave treatment, and Brazilian split-

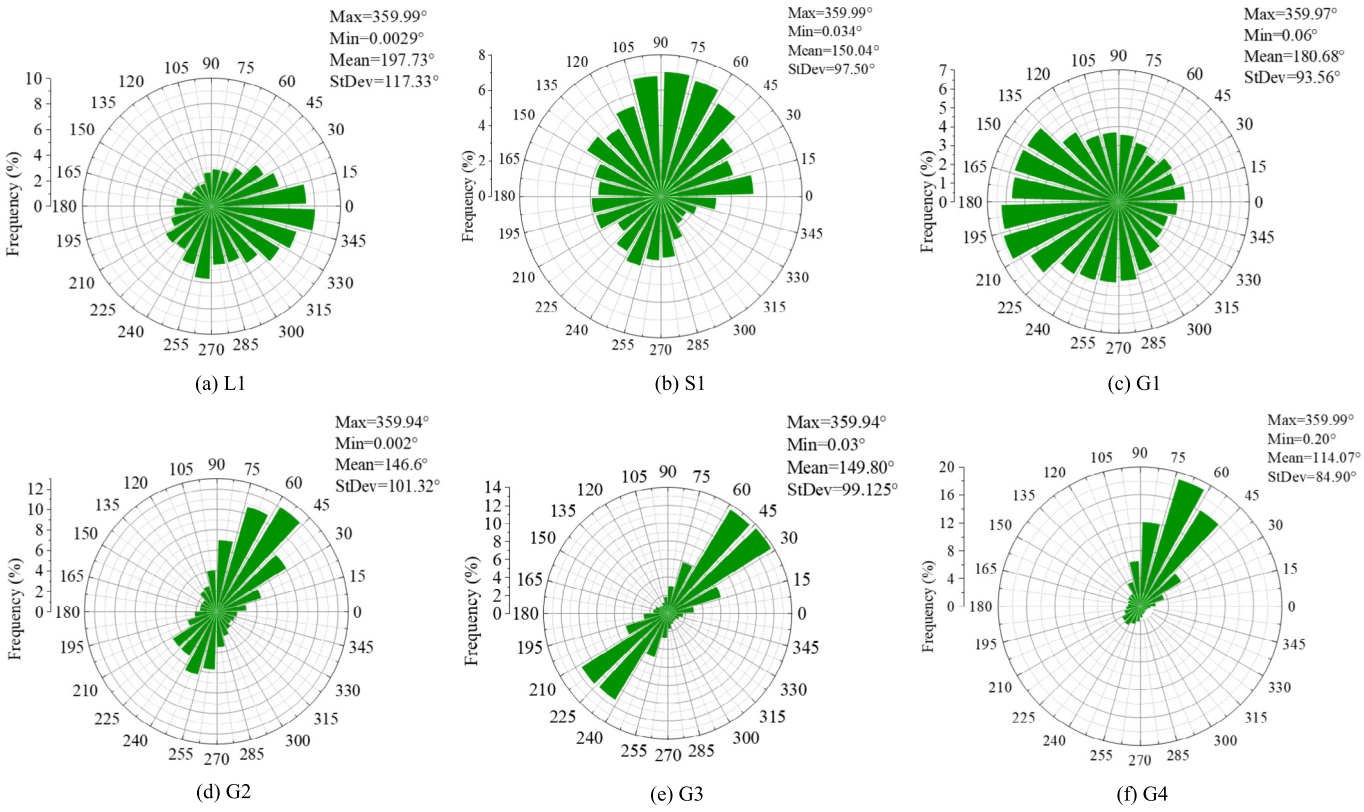

Fig. 10. Aspect angle of fracture surfaces within rocks.

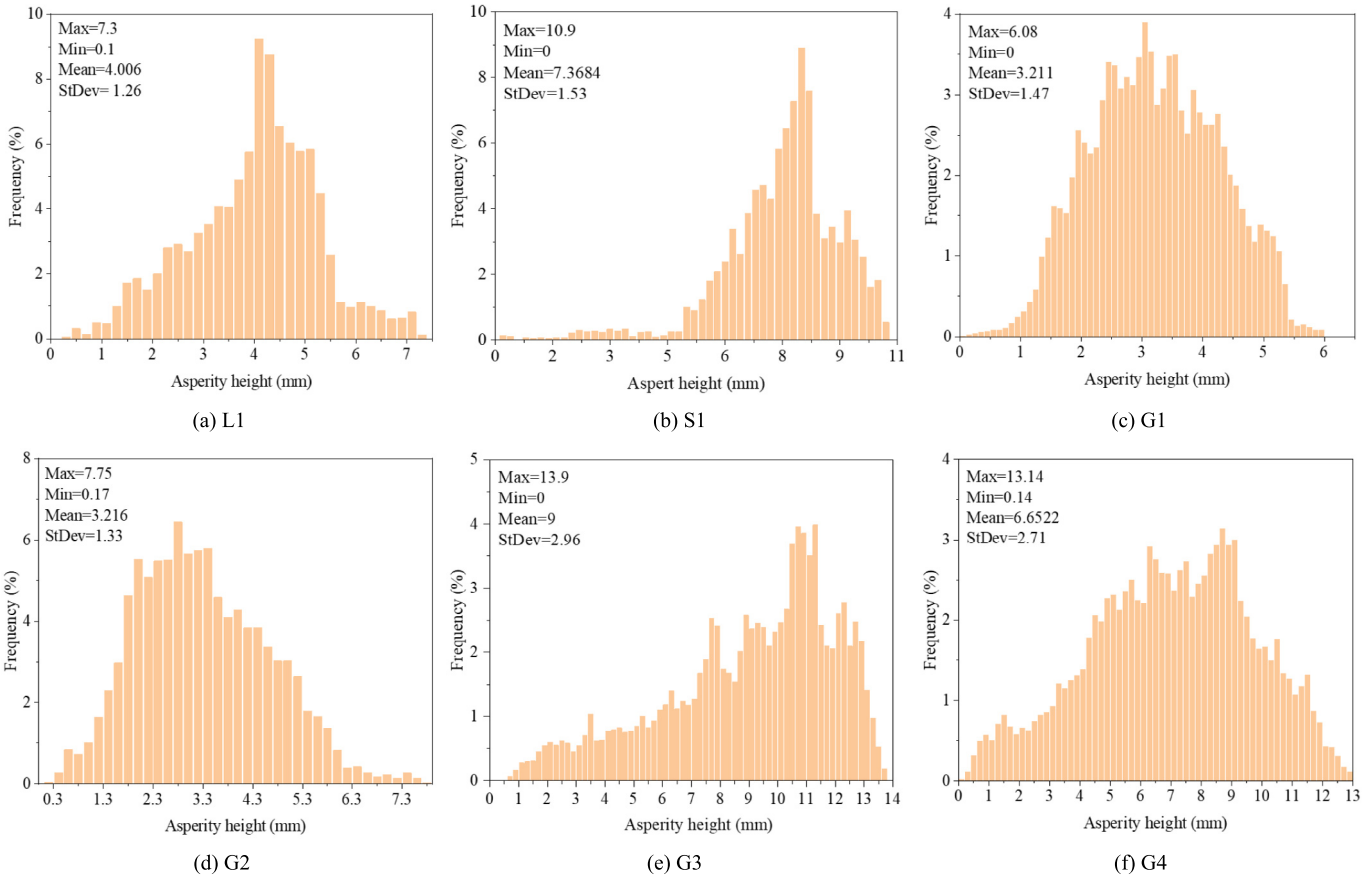

Fig. 11. Asperity height of fracture surface within rocks.

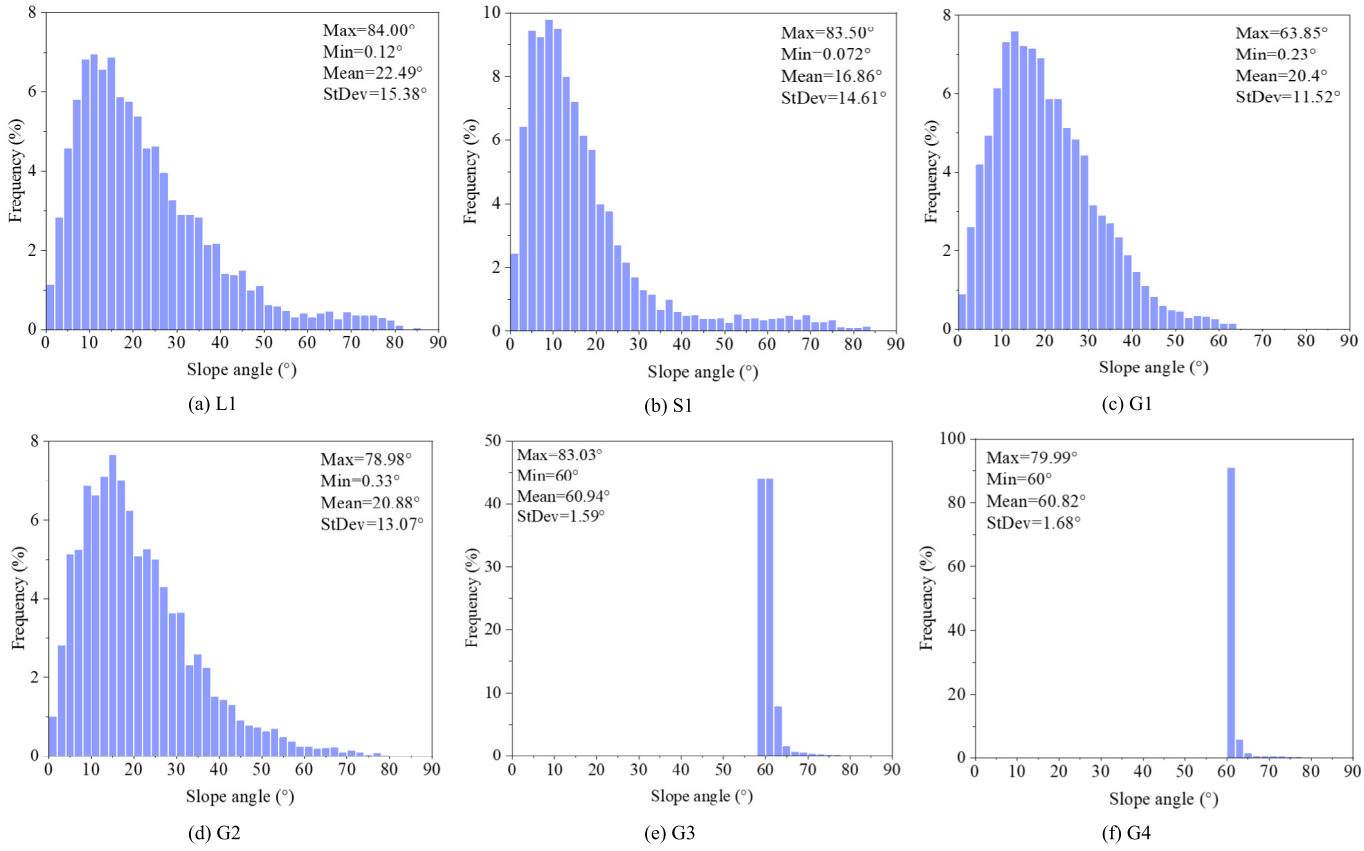

Fig. 12. Slope angle of fracture surface within rocks.

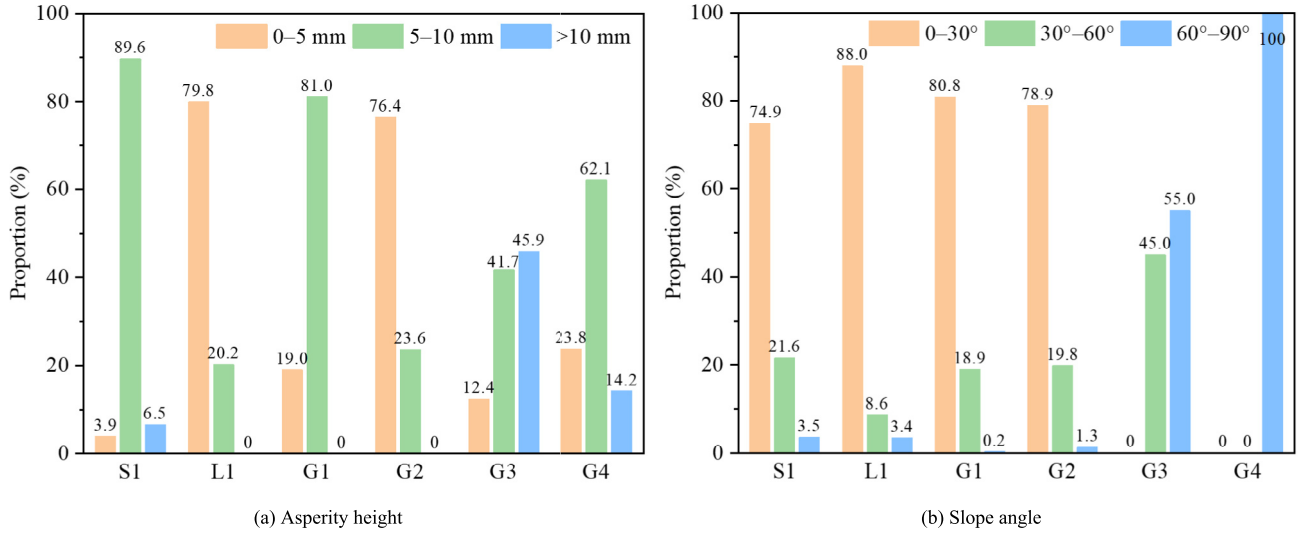

Fig. 13. Distribution of asperity height and slope angle.

ting under varying water saturation, respectively. Their findings demonstrated that the asperity heights of the fracture surfaces were distributed in the ranges from 0–9 mm, 0–7 mm, and 0–6.1 mm, respectively. According to the classification established in this study, these fracture surfaces are categorized as smooth and moderately rough surfaces. Interestingly, it was observed that the larger-sized rock fracture surfaces following laser irradiation reveal a higher extent of roughness.

As exhibited in Fig. 13b, the slope angle distribution of rock fracture surfaces is categorized into three classifications: low slope angle (0–30°), moderately slope angle (30°–60°), and high slope angle (60°–90°). The findings demonstrate that the proportion of slope angle distribution for fracture surfaces of specimens G1, S1, and L1 in the range of 0–30° accounts for 80.8%, 74.9%, and 88.0% respectively, indicating that these surfaces are classified as low dip angle fracture surfaces. Among the three types of rock samples, the sandstone surface

has the highest proportion of slope angle distribution in the 60°–90° range, at approximately 3.5%. Furthermore, the proportions of slope angles for the G3 and G4 fracture surfaces within the 60°–90° range are 55.0% and 100%, respectively, thereby categorizing them as high dip angle fracture surfaces.

Following laser irradiation, the smaller-sized limestone fracture surfaces are the flattest, classifying them as low dip angle smooth fracture surfaces. Meanwhile, the smaller-sized granite and sandstone fracture surfaces are categorized as low dip angle, moderately rough surfaces. The larger-sized granite fracture surfaces are classified as high-dip-angle rough fracture surfaces.

3.2.5. Anisotropy features

The Z_2 distribution in various orientations of rock fracture surfaces is examined, as represented in Fig. 14. Fig. 14a–c displays the Z_2 pattern in different directions of S1, L1, and G1 fracture surfaces. The Z_2 distribution of rock fracture surfaces exhibits pronounced anisotropic characteristics. For instance, the Z_2 values for the S1, L1, and G1 fracture surfaces are within the ranges of 0.59–3.08, 0.18–1.22, and 0.23–0.58, respectively. In addition, the fracture surfaces of sandstone, limestone, and granite display higher Z_2 values in the ranges of 60°–80°, 90°–130°, and 60°–105°, respectively. These findings reveal that the fracture surface of sandstone exhibits strong anisotropy under laser irradiation, followed by limestone and granite. The results can be attributed to the fact that both sandstone and limestone belong to sedimentary rock, characterized by loosely arranged internal mineral particles and numerous initial defects. These initial defects contribute to the irregularity of the microcrack propagation paths [34], resulting in a marked anisotropy of the fracture surface.

Fig. 14d–f illustrates the Z_2 distribution in G2, G3, and G4 fracture surfaces. The results point out that as the granite size increases from ϕ60 mm × 30 mm to ϕ100 mm × 50 mm, the distribution range of Z_2 across different orientations of the rock fracture surface also decreases. For example, the Z_2 values of the G2, G3, and G4 fracture surfaces are distributed within the range of 0.28–2.59, 0.2–1.24, and 0.3–0.67, respectively. Besides, the G2, G3, and G4 fracture surfaces demonstrate larger Z_2 values in the angular ranges of 60°–75°, 75°–120°, and 90°–170°, respectively. The larger the diameter of the rock specimen, the higher the ligament and thickness, thereby enhancing the heterogeneity of the rock specimen to a certain extent [39]. This variability ultimately influences the structure of rock fracture surfaces following laser irradiation.

R_z was employed to quantify the height of the fracture surface morphology, which refers to the vertical distance between the highest peak and the lowest valley within a sampling length. The R_z distribution in various orientations of fracture surfaces is represented in Fig. 15. Fig. 15a–c presents the R_z values for the S1, L1, and G1 fracture surfaces. It reveals that the sandstone fracture surface exhibits a higher R_z value and a broader distribution range compared to the granite and limestone fracture surfaces after laser irradiation. Specifically, the R_z distribution ranges for the S1, G1, and L1 fracture surfaces are 1.61–7.11 mm, 1.71–4.87 mm, and 3.76–5.55 mm, respectively. In addition, the fracture surfaces of specimens S1, G1, and L1 exhibit higher R_z values within the angular ranges of 120°–150°, 60°–90°, and 60°–115°, respectively. This observation suggests that the rock specimens undergo tensile damage due to laser-induced thermal shock, leading to greater height fluctuations in these specific directions [20]. Moreover, as stated by the research conducted by Gu et al. [19], local surfaces on rock fractures may exhibit greater roughness after thermal damage due to the anisotropy features of fracture surfaces, which is also observed in this study.

Fig. 15c–f depicts the R_z distribution in various directions for the G1, G2, G3, and G4 fracture surfaces. It is apparent that as the size of granite specimens increases from ϕ50 mm × 25 mm to ϕ100 mm × 50 mm, the dispersion of the R_z distribution on the rock fracture surfaces is enlarged. Specifically, the R_z values of G1, G2, G3, and G4 fracture surfaces fall within the ranges of 1.71–4.87 mm, 3.02–6.67 mm, 2.46–6.29 mm, 3.06–10.52 mm, and the standard deviations are 0.65, 0.86, 1.04, and 2.52, respectively. Additionally, it indicates that as the rock size increases, the influence of the size effect on the R_z distribution of fracture surfaces diminishes. Previous research of Mei et al. [42] supported this observation, establishing that when the specimen size was sufficiently large, the roughness of the rock fracture surface was apt to stabilize at a specific value. This indicates that as the rock size increases, the impact of anisotropy on the fracture surface is weakened.

3.3. Pore distribution and microstructure

3.3.1. Pore distribution

The NMR was employed to examine the pore distribution within rocks after laser irradiation in this study. To ensure the reproducibility of the experimental results, all samples were subjected to identical preparation and testing protocols, encompassing oven-drying, vacuum evacuation, water saturation, and NMR measurement. Fig. 16 exhibits the variation of pore size and pore content within the rock after laser irradiation. Fig. 16a illustrates the distribution of pore size in granite, sandstone, and limestone specimens. It reveals distinct differences in pore size distribution

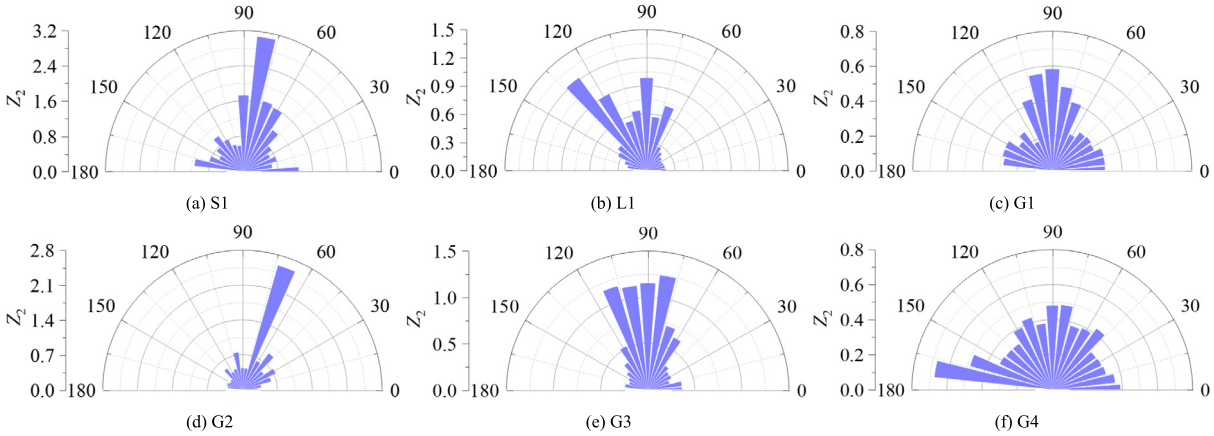

Fig. 14. Z_2 in different orientations for rock fracture surfaces.

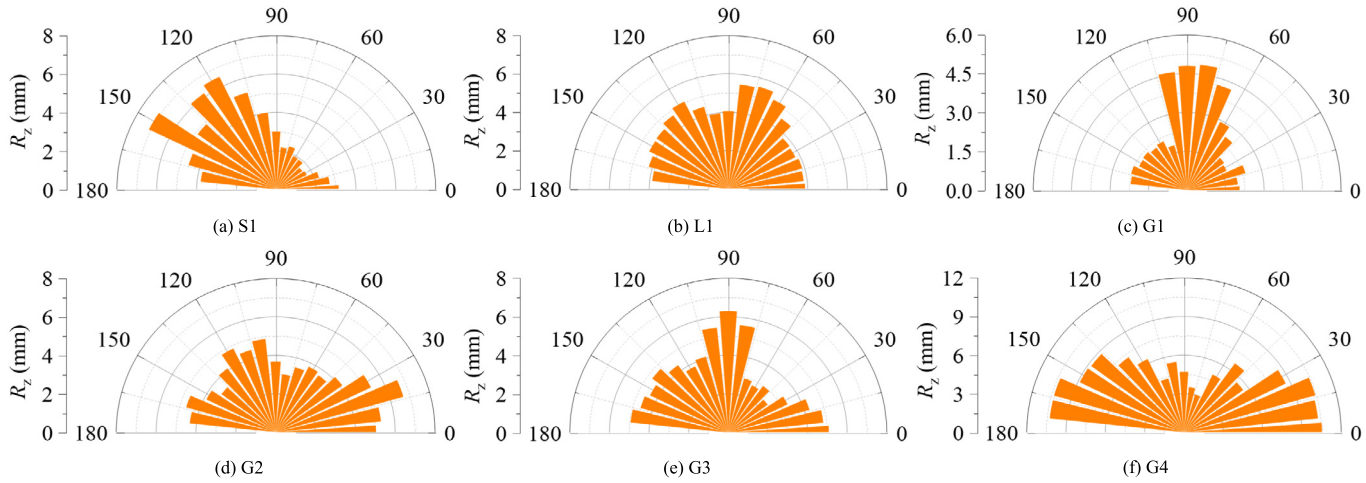

Fig. 15. R_z in different orientations for rock fracture surfaces.

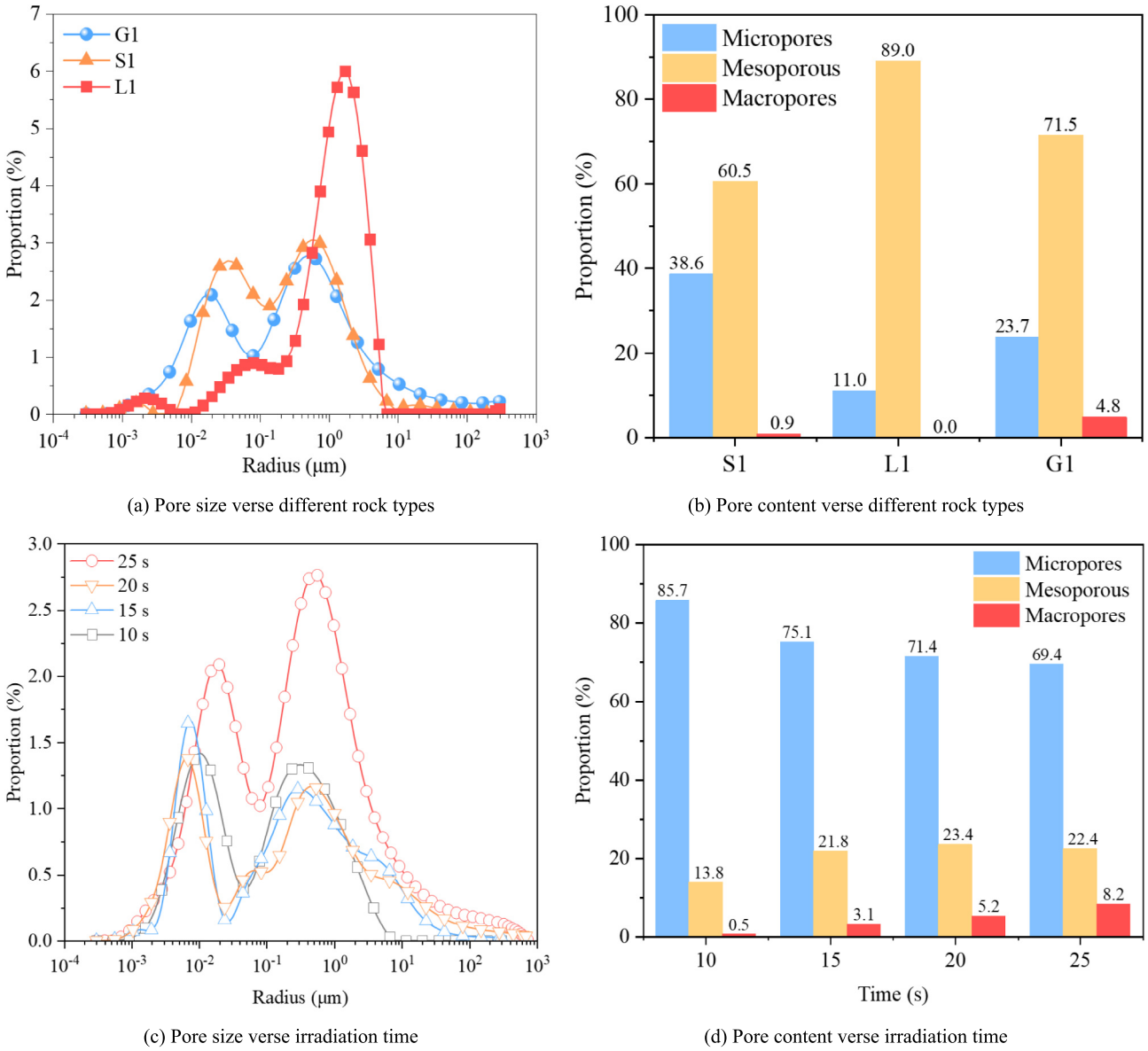

Fig. 16. Pore size and pore content distribution.

among the three types of rock samples following laser thermal shock. According to the study by Xi et al. [43], pores in rock can be categorized into three types based on their radii: micropores (0 μm < $r \leq$ 0.1 μm), mesopores (0.1 μm < $r \leq$ 1 μm), and macropores (r > 1 μm).

The pore distributions within rocks irradiated by laser are exhibited in Fig. 16b. The results reveal notable differences in pore content among the three types of rock samples. Sandstone exhibits the highest proportion of micropores, accounting for approximately 38.6% of its total pore volume. Granite contains the highest proportion of macropores, making up about 4.8% of its total pore volume. The mesopore content in limestone, granite, and sandstone is 89.0%, 71.5%, and 60.5%, respectively. This phenomenon can be explained as follows. Under thermally-induced stress, brittle mineral grains in both sandstone and granite are prone to fracture, producing microcracks that enhance the connectivity of previously isolated pores and expand the pore space [44]. Localized melting may induce abrupt volumetric changes or spallation, facilitating the formation of macroscopic cavities. As a result, macropore content is generally higher in sandstone and granite than in limestone. Moreover, the relatively loose and porous structure of sandstone provides more space for thermal deformation of minerals, which suppresses the growth of macropores [33]. Consequently, sandstone exhibits a lower macropore content compared to granite, while possessing a higher proportion of micropores.

Fig. 16c and d depict the variation in pore distribution in granite with varying irradiation time. The results clearly indicate that irradiation time exerts a significant influence on the pore content of granite. As irradiation time increases, the proportion of micropores decreases significantly, while the proportion of macropores increases gradually. For example, as the irradiation time increases from 10 to 25 s, the share of micropores in granite declines from 85.7% to 69.4%, while the share of macropores increases, spanning from 0.5% to 8.2%. This is mainly because with the extension of laser irradiation time, the physical and chemical changes of rock minerals are more thorough, and the thermal stress field is stronger. Consequently, enhanced compressive or tensile stresses between mineral grains facilitate pore coalescence and growth. According to Yang et al. [28], improved pore connectivity promotes the development of throats within the rock matrix. Furthermore, the frequent fluctuations of temperature differences and temperature gradients due to thermal shock induces mineral grains generate irreversible changes, increasing the complexity of pores and throat structures. These alterations foster the formation of an interconnected fracture network, enhancing both porosity and permeability.

At elevated temperatures, multiple mechanisms contribute directly to pore formation in rock, including water loss, mineral decomposition, phase transformations, chemical-bond rupture, microcrack development, and partial melting. Firstly, for granite and sandstone subjected to 200–500 °C, the release and evaporation of both free and structurally bound water cause mineral-volume expansion, facilitating the growth of micropores [29]. Secondly, at 500–1000 °C, the α- to β-quartz transition alters the Si—O bond angle and leads to volumetric expansion of quartz. Simultaneously, the phase transition of biotite mineral contributes to differential thermal expansion among minerals, further driving the conversion of micro- and mesopores into macropores. Thirdly, raised temperatures also bring about the rupture of chemical bonds in feldspar minerals (e.g., Ca—O, Al—O, K—O, Na—O) and in biotite (e.g., Fe—O, Mg—O), releasing CO_2 and destroying the mica lattice as hydroxyl groups escape and form albite. Feldspar-ion migration produces Frenkel and Vacancy defects, resulting in the increase of porosity—manifested by a reduction in micropore content and a rise in macropore proportion [29]. For limestone, the primary mineral is calcite. Calcite decomposes into white quicklime and other substances at roughly 700 °C. Furthermore, when the temperature achieves 900 °C, calcite undergoes cracking. These variations produce an increase in the internal pore volume of limestone.

3.3.2. Microstructure

Fig. 17 depicts the microstructure of granite, sandstone, and limestone. Fig. 17a presents the microstructure of melting region of limestone following laser irradiation. The results are evident that microcracks have developed in the melting region of limestone post-laser irradiation, and micropores can be seen locally, indicating that significant thermal damage has occurred inside the rock. According to the research of Wang et al. [33], the diffraction intensity of molten limestone minerals decreased substantially following laser irradiation, resulting in the ruin of the crystal structure and promoting thermally induced crack propagation along the bending path. This is owing to the fact that the thermal conduction inside limestone induces the thermal motion between mineral particles, resulting in rock layer separation and crack propagation [45]. As the microcracks inside the rock extend and interconnect, both the number and density of cracks increase, resulting in stress concentration at the crack tips. Once the thermal stress surpasses the tensile stress threshold of rock, tensile fractures occur, generating a smooth fracture surface, as illustrated in Fig. 17b.

Fig. 17c presents the microstructure of the melting region of sandstone following laser irradiation. The findings reveal a notably smooth melting region with extensive, interlaced microcracks, signifying severe microstructural damage from laser thermal shock. Fig. 17d further shows numerous micropores and debris in the thermally affected zone, with staggered, well-developed microcracks in the thermally affected region. This behavior is attributed to the aggregation and expansion of initial pores under the extrusion and tension of mineral grains. As heat conduction intensifies, the lattice stress within primary minerals (e.g., quartz and feldspar) increases sharply, resulting in the pores convergence at crack tips within the damage zone and facilitating the rapid formation of interconnected pore channels [28]. Simultaneously, the stress concentration at microdefect tips leads to the fracture and dislocations in the original interconnections between mineral particles. This process generates numerous angular particles, some of which are partially powdery. As a result, this alters the undulating state of the macroscopic fracture, resulting in the splitting of cemented particle clusters into rough fracture surfaces under tensile stress.

Fig. 17e exhibits the microstructure of the melting region of granite after laser irradiation. It is revealed that numerous well-rounded erosion pores and localized debris amid developed microcracks. Firstly, laser–induced thermal shock destroys the crystal clusters in granite, leading to the detachment and collapse of mineral particles. Secondly, the dehydration of the sample, along with the phase transformations of the constituent minerals, induces the generation of numerous pores and microcracks in the granite [46]. Thirdly, the increased density of pores and microcracks complicates the propagation paths of intergranular and transcrystalline cracks, enhancing the likelihood of tensile fractures. Ultimately, these processes result in the spalling of granite and the formation of a rough fractures surface, as depicted in Fig. 17f.

The results demonstrate that factors such as pore distribution, crack density, crack development trajectory, mineral particle separation, and the extent influenced by high temperature region significantly influence the roughness and anisotropy characteristics of rock fracture surface due to laser irradiation. Compared with sandstone and granite, limestone exhibits a lower degree of crack development, simpler crack trajectories, and a smoother post-irradiation microstructure. These factors affect the asperity height, slope angle and JRC distribution of the fracture surface of irradiated

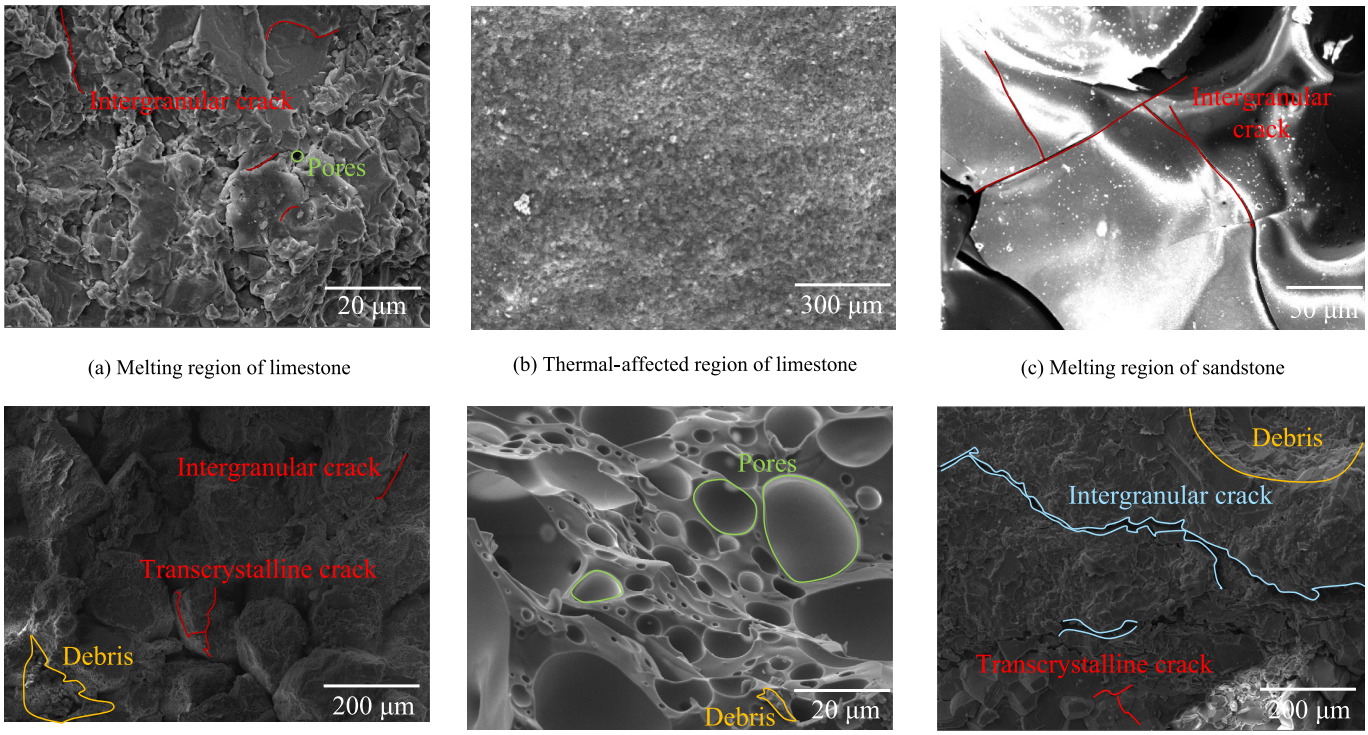

(a) Melting region of limestone

(b) Thermal-affected region of limestone

(c) Melting region of sandstone

(d) Thermal-affected region of sandstone

(e) Melting region of granite

(f) Thermal-affected region of granite

Fig. 17. Microstructure of irradiated rock specimens.

limestone. Additionally, researches have revealed that [47], larger rock specimens typically contain more initial defects, which facilitate tensile stress concentration and subsequent generate tensile fracture under laser thermal damage. However, increased specimen size also enhances the ligament and thickness and amplifies the heterogeneity of the rock. This is reflected in the fluctuating state, dip degree, and anisotropy difference of the macroscopic fracture surface within rock.

3.4. Fracture mechanism

The initiation and propagation of cracks in rocks under laser irradiation are driven by multiple interrelated mechanisms, including pore water evaporation, mineral phase transitions, melting, and thermal expansion, which ultimately result in the formation of macroscopic fractures. High temperatures induce the initiation of micro-defects within limestone due to thermal expansion of mineral crystals. As temperature increases, mineral crystal integrity is damaged, which promotes fracture and collapse of mineral grains and accelerates the propagation of microcracks [45]. The failure of limestone is strongly associated with the thermal decomposition of calcite, which produces CaO and releases CO_2. This reaction increases pore pressure and weakens intergranular cementation and frictional resistance. With further temperature rise, limestone exhibits enhanced plastic deformation, a sharp decline in load-bearing capacity, and a pronounced decrease in shear strength. These alterations result in pronounced shear failure characteristics [45].

For sandstone, high temperatures induce the thermal expansion among minerals, which generates intergranular compression and tension and promotes microcrack initiation and expansion. Sandstone generally contains numerous heterogeneous microscale defects. These defects and thermal cracks become initiation sites for macroscopic fractures [48]. Furthermore, when temperatures exceed 600 °C, a series of processes are triggered: mineral phase transformations, continued thermal expansion, and the decomposition of cementing materials. These processes generate grain spallation, intergranular sliding, and dislocations, all of which contribute to the formation of shear cracks [48]. This can explain why sandstone exhibits a higher proportion of shear cracks than granite. Since the primary minerals in the sandstone employed in this study are quartz and plagioclase, tensile failure induced by thermal expansion remains the dominant fracture mechanism.

For granite, the mismatch in thermal expansion among minerals is the principal driver for crack initiation and propagation. At temperatures above 600 °C, the thermal expansion coefficient of quartz is approximately 4 times that of feldspar. Microcracks width can reach 10 μm, while spalling defects may extend up to 348 μm [19]. Granite has a dense structure. As the temperature rises, expansion stresses exceeded the crystal's ultimate strength, which produced crystal damage and roughened crystal surfaces. Strongly cemented particle clusters separate under tensile stress, leading to increased crack density. This process promotes grain spalling and the interconnection of crack networks. With further crack propagation, the rock underwent tensile failure and generated rough fracture surfaces [20]. Additionally, fracture surfaces formed under melting-induced failure exhibit higher roughness, with fractal dimensions increasing by up to 2% compared to spalling fractures [49]. Therefore, when rock failure occurs mainly through spalling, the energy required for rock breakage is reduced, which is beneficial for hard rock excavation in tunneling engineering.

This study provides a preliminary investigation into the mechanisms of laser-induced rock fracturing. Currently, investigations are significantly constrained by the laser power and sample size. Future studies can focus on experiments with higher-power laser systems and larger-scale samples. Multi-parameter analyses should be applied to identify the critical characteristics of rock failure under laser irradiation. The evolution of crack propagation can be further investigated by integrating acoustic emission localization, CT scanning, and digital image correlation techniques. In

addition, the underlying mechanism of rock breaking by laser irradiation, combined with mechanical cutters, should be explored. These efforts could provide a solid theoretical foundation for the application of laser technology in hard rock fragmentation.

4. Conclusions

In this study, the failure mode and fracture characteristics of limestone, sandstone, and granite samples induced by laser irradiation were experimentally investigated. The roughness of the fracture surface was quantitatively characterized by JRC, fractal dimension, aspect angle, asperity height, and slope angle. The variation and damage mechanisms of the microstructure of rock after laser irradiation were revealed from the perspective of pore distribution and microstructure characteristics. The conclusions are summarized as follows:

(1) The acoustic emission energy curve of sandstone exhibits oscillatory behavior, followed by granite, while limestone displays a smoother acoustic emission signature. The peak acoustic emission energy of limestone achieved 3008.6 mV/μs. Under laser irradiation, limestone undergoes tension-shear composite failure, while granite and sandstone are dominated by tensile failure. As the time required for rock failure increases, the failure mode transitions from tensile-dominated to tension-shear composite failure.

(2) Both the JRC and the fractal dimension of laser-irradiated rock fracture surfaces decrease with an increase in sampling intervals. The JRC and fractal dimension of sandstone fracture surface surpass that of granite, which in turn exceeds those of limestone. The larger the specimen size, the higher the JRC and fractal dimension. The fracture surfaces of S1, G1, and L1 exhibit higher R_z within the angular ranges of 120°–150°, 60°–90°, and 60°–115° due to the rock specimens undergoing tensile damage after laser irradiation.

(3) After laser irradiation, the maximum asperity height of G3 and G4 fracture surfaces exceeded 13 mm, and the average slope angle and average aspect angle exceeded 60.5° and 110°. L1 fracture surface belongs to the low dip angle and smooth fracture surface, the G1, G2, and S1 fracture surface is attributed to the low dip angle and medium rough surface, and the G3 and G4 fracture surfaces belong to the high dip angle and rough fracture surface.

(4) The content of micropores in sandstone is higher than that of limestone and granite following laser irradiation, accounting for 38.6% of the total pore content. With the extension of irradiation duration, the proportion of macropore content in granite increased from 0.5% to 8.2%. Following laser thermal shock, the micropores and mesopores in the rock are transformed into macropores, and the pore expansion and connectivity promote the microcrack development.

Acknowledgements

This study was supported by Yunlong Lake Laboratory of Deep Underground Science and Engineering Project (No. 104023006), and National Key Research and Development Program of China (No. 2024YFF0507903).

References

[1] Panthi KK, Nilsen B. Predicted versus actual rock mass conditions: A review of four tunnel projects in Nepal Himalaya. Tunn Undergr Space Technol 2007;22(2):173–84.
[2] Zheng YL, He L. TBM tunneling in extremely hard and abrasive rocks: Problems, solutions and assisting methods. J Cent South Univ 2021;28(2):454–80.
[3] Zhou ZL, Dong JP, Wang SF, Cai X, Zhou K. Typical difficulties and improvement measures in TBM excavation of hard rock tunnels. Chin J Nonferrous Met 2023;33(4):1297–317.
[4] Wang HG, Huang HC, Bi WX, Ji GD, Zhou B, Zhuo LB. Deep and ultra-deep oil and gas well drilling technologies: Progress and prospect. Nat Gas Ind B 2022;9(2):141–57.
[5] Wang YJ, Yu DX, Wang ZG, Chu ZX, Zhao GS, Zhou GQ. Experimental research on thermal cracking and mechanical properties of granite irradiated by laser beam. J China Univ Min Technol 2023;52(4):701–12.
[6] Wang YJ, Jiang JY, Darkwa J, Xu ZY, Zheng XF, Zhou GQ. Experimental study of thermal fracturing of hot dry rock irradiated by moving laser beam: Temperature, efficiency and porosity. Renew Energy 2020;160:803–16.
[7] Li MY, Han B, Zhang SY, Song LX, He QK. Numerical simulation and experimental investigation on fracture mechanism of granite by laser irradiation. Opt Laser Technol 2018;106:52–60.
[8] Li Q, Zhai YL, Huang Z, Chen K, Zhang WL, Liang YW. Research on crack cracking mechanism and damage evaluation method of granite under laser action. Opt Commun 2022;506:127556.
[9] Chen K, Huang ZQ, Deng R, Zhang WL, Kang MQ, Ma YC, Shi MJ, Yan J. Research on the temperature and stress fields of elliptical laser irradiated sandstone, and drilling with the elliptical laser-assisted mechanical bit. J Pet Sci Eng 2022;211:110147.
[10] Wang YJ, Shi YL, Jiang JY, Zhou GQ, Wang ZG. Experimental study on modified specific energy, temperature field and mechanical properties of Xuzhou limestone irradiated by fiber laser. Heat Mass Transf 2020;56(1):161–73.
[11] Feng XW, Huang P, Carvelli V, Lin GS, Zhu CK, He FZ. Can laser irradiation improve the strength of weak rock mass? J Rock Mech Geotech Eng 2024;17(1):139–53.
[12] Gao MZ, Liu JJ, Li CX, Yang BG, Li F, Zhou XM, Yang L, Yang ZD, Xie J. Damage and fracture behavior and spatio-temporal evolution of acoustic emission of sandstone before and after laser radiation. J Cent South Univ 2024;31(9):3264–80.
[13] Zhou XM, Hao HC, Liu JJ, Yang L, Yang ZD, Wang X, Gao Z, Wu Y, Gao MZ. Mechanism of increasing or inhibiting laser-weakened rocks by saturated fluids and mechanical behavior of rocks after laser damage. Eng Fract Mech 2023;293:109723.
[14] Shi ZM, Li JT, Ranjith PG, Wang MX, Lin H, Han DY, Li KH. Acoustic emission and fracture morphology characteristics of thermal-damage granite under mixed mode I/III loading. Theor Appl Fract Mech 2024;133:104524.
[15] Wang QY, Wang DB, Li XH, Hou YH, Sheng M, Long LQ, Wang YL, Yu B. Experimental investigation on the elastic-plastic failure evolution mechanism of high-temperature hot dry rocks using combined monitoring of acoustic emission and digital image correlation. Geothermics 2025;131:103359.
[16] Qin WJ, Zhao YQ, Jin AB, Chen SJ, Liu JB. Analysis of precursor and failure mechanisms of granite under high temperature: Based on acoustic emission and 3D-DIC perspectives. Constr Build Mater 2025;473:141049.
[17] Kumar Singh S, Pratap Banerjee B, Raval S. A review of laser scanning for geological and geotechnical applications in underground mining. Int J Min Sci Technol 2023;33(2):133–54.
[18] Gao M, Zhang CG, Oh J. Assessments of the effects of various fracture surface morphology on single fracture flow: A review. Int J Min Sci Technol 2023;33(1):1–29.
[19] Gu QX, Huang Z, Zhao K, Zhong W, Liu L, Li SJ, Ma D, Liu Q. Experimental investigation on the influence of temperature on the fracture surface variations of granite after Brazilian splitting tests. Int J Therm Sci 2024;203:109159.
[20] Gu QX, Huang Z, Zhao K, Zhong W, Liu L, Li XZ, Wu Y, Dan M. Effects of high temperature and thermal cycles on fracture surface's roughness of granite: An insight on 3D morphology. J Rock Mech Geotech Eng 2024;17(2):810–26.
[21] Li BX, Yu S, Yang L, Zhu WS, Xue YG, Feng D, Wang C, Chen YJ. Multiscale fracture characteristics and failure mechanism quantification method of cracked rock under true triaxial compression. Eng Fract Mech 2022;262:108257.
[22] Yang BG, Xie J, Yang YM, Liu JJ, Ye SQ, Tang RF, Gao MZ. Anisotropy and size effect of the fractal characteristics of rock fracture surfaces under microwave irradiation: An experimental research. Fractals 2024;32(4):2340123.
[23] Yang Z, Tao M, Memon MB, Zhuang DD, Zhao Y. Microwave irradiation-induced deterioration of rock mechanical properties and implications for mechanized hard rock excavation. J Rock Mech Geotech Eng 2024;17(1):275–90.
[24] Aghababaei M, Behnia M, Aliha MRM. Experimental investigation on the effect of grain size of granitic rocks on the fracture roughness and toughness. Geomech Energy Environ 2024;38:100535.
[25] Pan HZ, Kang Y, Hu Y, Liu F, Xu JJ, Li D, Li JM. Determination of the property evolution in rock after laser irradiation by nanoindentation and nuclear magnetic resonance. Int J Rock Mech Min Sci 2024;174:105638.
[26] Wu B, Liu L, Yu DX, Wang JZ, Wang YJ. Experimental study on tensile strength and pore distribution of granite by laser irradiation. Min Constr Technol 2024;45(4). 88–94+74.
[27] Zhang Y, Gao YN, Yu LY. Multi-stage evolution of pore structure of microwave-treated sandstone: Insights from nuclear magnetic resonance. Int J Rock Mech Min Sci 2024;183:105952.
[28] Yang XX, Yu BP, He SX, Dong YS, Xin GX. Fracture characteristics and pore connectivity of sandstone under thermal shock. Chin J Geotech Eng 2022;44(10):1925–34.

[29] Gu C, Geng JS, Sun Q, Zhang YL, Hu JJ. Effect of water on granite deterioration under microwave radiation based on real-time AE monitoring. Rock Mech Rock Eng 2024;57:11399–412.
[30] Cao RH, Wang CS, Hu T, Yao RB, Li TB, Lin QB. Experimental investigation of plane shear fracture characteristics of sandstone after cyclic freeze-thaw treatments. Theor Appl Fract Mech 2022;118:103214.
[31] Liu JJ, Zhang C, Yang L, Zhou XM, Xie J, Yang BG, He ZQ, Gao MZ. Experimental and simulation studies on damage characteristics, crack development patterns, and strength reduction mechanisms of sandstone under laser irradiation. Geomech Geophys Geo-Energy Geo-Resour 2024;10(1):147.
[32] Xie HX, Xie HP, Zhang ZT, Yao QL, Cao ZG, Gao H, Shan CH, Yan ZW, Yin RJ. Fatigue fracture behaviors and damage evolution of coal samples treated with drying-wetting cycles investigated by acoustic emission and nuclear magnetic resonance. Int J Rock Mech Min Sci 2025;185:105976.
[33] Wang YJ, Yu DX, Sun LP, Zhu QY, Wang JZ. Thermal-breaking characteristics and crack distribution of rock irradiated by laser beam. Chin J Geotech Eng 2024;46(9):1809–19.
[34] Xue Y, Li X, Liu J, Ranjith PG, Gao F, Cai CZ, Xie HP, Cao ZZ. An experimental study on mechanical properties and fracturing characteristics of granite under high-temperature heating and liquid nitrogen cooling cyclic treatment. Geoenergy Sci Eng 2024;237:212816.
[35] Xu XH, Bao H, Lan HX, Liu CQ, Xu JB, Yan CG. Sampling interval-size effects and differential sensitivities of different morphology parameters of rock joint. J Struct Geol 2022;155:104530.
[36] Zhang C, Wang XJ, Shi XT, Zhao YX, Han PH, Zhang T. Splitting characteristics of sandstone under the influence of water saturation and its mechanism of water rock interaction. Chin J Rock Mech Eng 2024;43(S2):3722–37.
[37] Xue Y, Zhang JH, Liu J, Shi XY, Cai CZ, Zhang ZZ, Gao F, Zhang Y. Characteristics of Brazilian splitting failure and acoustic emission evolution of high-temperature coal after liquid nitrogen cooling treatment. Adv Eng Sci 2025;57(1):177–88.
[38] Wang HH, Zhou L, Zhu ZM, Shui X, Nie FK, Zhang HD, Liu JJ. Study on the effect of heating rate and temperature on the fracture properties of flawed granite. Theor Appl Fract Mech 2024;133:104584.
[39] Pérez-Rey I, Muñoz-Ibáñez A, González-Fernández MA, Muñiz-Menéndez M, Herbón Penabad M, Estévez-Ventosa X, Delgado J, Alejano LR. Size effects on the tensile strength and fracture toughness of granitic rock in different tests. J Rock Mech Geotech Eng 2023;15(9):2179–92.
[40] Wu QH, Weng L, Zhao YL, Guo BH, Luo T. On the tensile mechanical characteristics of fine-grained granite after heating/cooling treatments with different cooling rates. Eng Geol 2019;253:94–110.
[41] Zhang C, Wang XJ, Han PH, Zhang T, Zhang L, Wang FT. Acoustic emission and splitting surface roughness of sandstone in a Brazilian splitting test under the influence of water saturation. Eng Geol 2024;329:107369.
[42] Mei QW, Chen G, Luo FQ, Ma L, Gong HS, Long YZ. Research on size effect and directionality of roughness of natural rock fracture surface. Gold Sci Technol 2024;32(2):290–305.
[43] Xi Y, Xing JH, Jiang HL, Chen YC, Li J, Fan LF. Experimental study on pore characteristics evolution and rock damage mechanism of thermal-cooling treated sandstone. Constr Build Mater 2024;440:137498.
[44] Wu H, Wang YH, Tan JQ, Ma X, Hu RN, Liu WH. Influences of lithofacies on fluid mobility in mixed sedimentary rocks: Insights from NMR analysis of the middle Permian Lucaogou Formation, Junggar Basin. Energy Geosci 2024;5(4):100305.
[45] Zhang LY. Properties of failure mode and thermal damage for limestone at high temperature. Min Sci Technol (China) 2009;19(3):290–324.
[46] Hu XJ, Yu Y, Lacidogna G, Gong XN. The influence of temperatures on the mechanical properties and fracture behavior of rocks under mixed mode I/II loading. Eng Fract Mech 2024;309:110399.
[47] Alireza D, Hamed M. Specimens size effect on mechanical and fracture properties of rocks: a review. J Min Environ 2023;14(4):1273–93.
[48] Xiao WJ, Zhang D, Luo WJ, Huang YH, Wan H, Li SJ. Influence of temperature on building sandstone: Insights from microstructure, thermal strain and rupture crack. Constr Build Mater 2024;451:138888.
[49] Gao MZ, Xie J, Yang BG, Tang RF, Deng HC, Liu YT, Ye SQ, Zhou XM, Lan WS. Characteristics and mechanism of rock 3D volume fracturing in microwave field. J China Coal Soc 2022;47(3):1122–37.